

## STEADY-STATE PLANET MIGRATION BY THE KOZAI-LIDOV MECHANISM IN STELLAR BINARIES

CRISTOBAL PETROVICH<sup>1</sup>*Draft version June 22, 2018*

## ABSTRACT

We study the steady-state orbital distributions of giant planets migrating through the combination of the Kozai-Lidov (KL) mechanism due to a stellar companion and friction due to tides raised on the planet by the host star. We run a large set of Monte Carlo simulations that describe the secular evolution of a star-planet-star triple system including the effects from general relativistic precession, stellar and planetary spin evolution, and tides. Our simulations show that KL migration produces Hot Jupiters (HJs) with semi-major axes that are generally smaller than in the observations and they can only explain the observations if the following are both true: (i) tidal dissipation at high eccentricities is at least  $\sim 150$  times more efficient than the upper limit inferred from the Jupiter-Io interaction; (ii) highly eccentric planets get tidally disrupted at distances  $\gtrsim 0.015$  AU. Based on the occurrence rate and semi-major axis distribution of HJs, we find that KL migration in stellar binaries can produce at most  $\sim 20\%$  of the observed HJs. Almost no intermediate-period (semi-major axis  $\sim 0.1 - 2$  AU) planets are formed by this mechanism—migrating planets spend most of their lifetimes undergoing KL oscillations at large orbital separations ( $> 2$  AU) or as Hot Jupiters.

## 1. INTRODUCTION

1.1. *Planets in binary systems*

Current observations show that  $\sim 20\%$  of exoplanet host stars are in binary (or even higher order) stellar systems (Desidera & Barbieri 2007; Mugrauer & Neuhäuser 2009; Raghavan et al. 2010). The observed gas giant planets in such binary systems seem to reside preferentially in close-in orbits ( $< 0.1$  AU) and have large masses relative to the planets in single stars (Zucker & Mazeh 2002; Udry & Santos 2007; Law et al. 2014). Also, the binary systems harboring giant planets have preferentially wide orbital separations ( $> 100$  AU) (Eggenberger et al. 2011). These findings suggest that wide stellar companions may play a significant role at shaping the planetary orbits of giant planets.

It might be expected that the protostellar accretion disks in binary stars form in alignment with the orbit of the binary if its semi-major axis is not too large. Moreover, since the stars accrete high angular momentum gas from the protostellar disks their spins can also be brought into alignment with the binary orbit and the accretion disk. By measuring the inclination to the line of sight of the spin of the stars in binaries Hale (1994) inferred that binaries with semi-major axes  $\lesssim 30 - 40$  AU are spin-aligned, while at larger separations the spin vectors become randomly oriented relative to each other. This result suggests that protostellar disks, in which planets will ultimately form, have angular momentum vectors that are not correlated with the angular momentum vector of the binary for wide enough binary separations. Note, however, that polarimetry studies of protostellar disks find that the disks in individual stars in binaries are preferentially aligned with each other for binary separations up to a few hundred AU (Jensen et al. 2004; Monin et al. 2006). More recently, ALMA observations have revealed protoplanetary disks in wide (separations

of  $\sim 400$  AU) binaries are misaligned by  $\sim 60 - 80$  degrees (Jensen & Akeson 2014; Williams et al. 2014).

An important assumption we make throughout this work is that the angular momentum of the binary and that of the planetary system are uncorrelated for semi-major axis  $> 100$  AU.

1.2. *The Kozai-Lidov mechanism*

The long-term stability of star-planet-star system requires that the system is hierarchical ( $a_{\text{in}} \ll a_{\text{out}}$ ) and that the eccentricity of the outer binary  $e_{\text{out}}$  is small enough so the inner and outer orbits do not experience close approaches (e.g., Holman & Wiegert 1999). In such systems, a large mutual inclination between the inner and outer orbits can produce large-amplitude oscillations of the eccentricity and inclination; this is the so-called Kozai-Lidov (KL) mechanism (Kozai 1962; Lidov 1962). Such oscillations have a characteristic timescale (Holman et al. 1997)

$$\tau_{\text{KL}} = \frac{2P_{\text{out}}^2}{3\pi P_{\text{in}}} \frac{m_1 + m_2 + m_3}{m_3} (1 - e_{\text{out}}^2)^{3/2}, \quad (1)$$

where  $m_1$  and  $m_2$  are the masses of the inner binary (host star and planet), while  $m_3$  is the mass of the perturber (stellar companion). The inner binary has a period  $P_{\text{in}}$ , while the outer binary has a period and eccentricity  $P_{\text{out}}$  and  $e_{\text{out}}$ .

KL cycles can be studied analytically by averaging over the orbital phases of the inner and outer binaries (usually called the secular approximation) (Kozai 1962; Ford et al. 2000), which is generally a good approximation because the precession time is much longer than the orbital period of either binary (although see Antognini et al. 2014 and discussion in §10.2.4). Under the secular approximation the semi-major axis of the inner binary  $a_{\text{in}}$  and outer binary  $a_{\text{out}}$  are both conserved.

The perturbing potential of the outer companion can be written in the quadrupole approximation (expansion up to  $a_{\text{in}}^2/a_{\text{out}}^3$ ) in the limiting case when  $a_{\text{in}} \ll$

<sup>1</sup> Department of Astrophysical Sciences, Princeton University, Ivy Lane, Princeton, NJ 08544, USA; cpetrovi@princeton.edu

$(1 - e_{\text{out}})a_{\text{out}}$ , which implies the following important results: (i) this averaged potential is axisymmetric relative to the orbital plane of the outer binary and so the angular momentum of the inner binary along this symmetry axis is conserved; (ii) the Hamiltonian describing the evolution of the system is integrable (it has one degree of freedom); (iii) the eccentricity of the outer binary  $e_{\text{out}}$  remains constant.

These results break down when higher order terms are included in the potential. In particular, when expanding up to the octupole approximation and considering an eccentric perturber ( $e_{\text{out}} > 0$ ) the potential is no longer axisymmetric and the corresponding Hamiltonian has two degrees of freedom. Recent work by Katz, Dong, & Malhotra (2011), Lithwick & Naoz (2011), and Naoz et al. (2013a) show that under such conditions the KL oscillations are modulated on timescales that are longer than  $\tau_{\text{KL}}$  in Equation (1) (by a factor of  $\sim \epsilon_{\text{oct}}^{-1}$  with  $\epsilon_{\text{oct}} = \frac{25}{16} \frac{a_{\text{in}}}{a_{\text{out}}} \frac{e_{\text{out}}}{(1 - e_{\text{out}}^2)} \frac{m_1 - m_2}{m_1 + m_2}$  in Eq. [A3]). This longer-timescale modulation can give rise to a more dramatic orbital evolution of the inner orbit, which includes episodes of extremely high eccentricities and orbit flipping between retrograde and prograde relative to the angular momentum vector of the outer binary. Moreover, provided that the angular momentum of the outer orbit is not much larger than the angular momentum of the inner orbit, the eccentricity of the perturber does not necessarily remain constant (e.g., Naoz et al. 2011).

The KL cycles are driven by the interplay between the weak tidal torque from the outer orbit and the shape of the inner orbit. Thus, such cycles can be suppressed by extra forces that lead to pericenter precession (see the precession rates  $Z_1$ ,  $Z_2$ , and  $Z_{\text{GR}}$  in Appendix A) in a timescale shorter than (or comparable to)  $\tau_{\text{KL}}$  in Equation (1) (e.g., Wu & Murray 2003; Fabrycky & Tremaine 2007).

In the context of KL migration general relativistic (GR) precession is generally able to suppress the oscillations at the largest distances because the GR precession rate  $Z_{\text{GR}}$  in Eq. [A17] has the weakest dependence on  $a_{\text{in}}$  compared to the other precession forces. If the planetary orbit starts from  $e \sim 0$  then GR precession suppresses the KL cycles when  $\tau_{\text{KL}} Z_{\text{GR}} \sim 1$  (Fabrycky & Tremaine 2007; Dong et al. 2014), which happens at a semi-major axis

$$a \sim 2.5 \text{ AU} \left( \frac{m_1}{M_\odot} \right)^{1/2} \left( \frac{m_3}{M_\odot} \right)^{-1/4} \left( \frac{a_{\text{out}} \sqrt{1 - e_{\text{out}}^2}}{1000 \text{ AU}} \right)^{3/4} \quad (2)$$

If the planetary orbits reaches a maximum eccentricity  $e_{\text{max}}$  that allows for migration down to a final semi-major axis  $a_{\text{F}} = a(1 - e_{\text{max}}^2)$ , the KL oscillations are quenched once the planet migrates to a semi-major axis (Socrates et al. 2012b):

$$a_{\text{Q}} \sim 2 \text{ AU} \left( \frac{a_{\text{F}}}{0.05 \text{ AU}} \right)^{-1/7} \left( \frac{m_1}{M_\odot} \right)^{4/7} \left( \frac{m_3}{M_\odot} \right)^{-2/7} \left( \frac{a_{\text{out}} \sqrt{1 - e_{\text{out}}^2}}{1000 \text{ AU}} \right)^{6/7}, \quad (3)$$

thereafter the eccentricity and semi-major axis decay at constant angular momentum.

### 1.3. Previous work on KL migration

Based on the formalism developed by Eggleton et al. (1998) and Kiseleva et al. (1998) for KL cycles with tidal friction, Wu & Murray (2003) carried out the first calculation of planet migration as a plausible explanation of history of the very eccentric ( $e = 0.93$ ) planet HD 80606b. Such migration ends with the formation of a Hot Jupiter: a gas giant planet with semi-major axis  $< 0.1 \text{ AU}$ .

Subsequent work by Fabrycky & Tremaine (2007) and Wu et al. (2007) study the orbital distributions of Hot Jupiters that arise from KL migration by building a large number of star-planet-star systems. In particular, Fabrycky & Tremaine (2007) show that HJs formed by KL migration have orbits that are commonly misaligned with respect to the spin axes of their host stars, which has been observed for many HJ systems (e.g., Albrecht et al. 2012). A major limitation of this work is that the authors consider a population of stellar perturbers with a fixed semi-major axis and zero eccentricity (similar to our simulation SMA500e0 in Table 1), which is not representative of the observed binary population. In contrast, Wu et al. (2007) do consider a population of perturbers based on the observed binary distributions, which allows them to estimate that KL migration might account for  $\sim 10\%$  of the observed HJs.

The studies by Fabrycky & Tremaine (2007) and Wu et al. (2007) have modeled the gravitational interactions by using the secular approximation, expanding the potential up to quadrupole approximation. As discussed in §1.2, such approximation might be inaccurate for eccentric binaries for which  $a_{\text{in}}/a_{\text{out}}$  is not  $\ll 1$ . Indeed, Naoz et al. (2012) show that by considering the octupole-level gravitational interactions the efficiency to produce HJs increases considerably (a factor of  $\sim 4 - 6$ ) relative to the Monte Carlo simulations by Wu et al. (2007), while the obliquity distribution of HJs broadens relative to that predicted by Fabrycky & Tremaine (2007).

All these studies of KL migration focus on the final states of the planetary systems: the simulations after several Gyrs or when the planet has either migrated or been tidally disrupted. Our approach is somewhat different because we study the steady-state distribution of the planetary orbital elements due to KL migration. This allows us to study the formation of not only HJs, but also migrating planets at wider separations.

### 1.4. Constraints on tidal dissipation

The orbital period of the Jupiter-Io system is shorter than Jupiter's spin period (super-synchronous rotation). Assuming that the outward migration of Io to its current location occurs within 4.5 Gyr constrains the maximum amount of dissipation in Jupiter, which in terms of the quality factor<sup>2</sup>  $Q_{\text{J-I}} > 5.9 \times 10^4$  (Goldreich & Soter 1966; Yoder & Peale 1981; Leconte et al. 2010), close to the measurement of  $Q_{\text{J-I}} = (3.56 \pm 0.66) \times 10^5$  using astrometric observations of the Galilean moons (Lainey et al. 2009). This upper limit to the amount of dissipation of  $Q_{\text{J-I}} > 5.9 \times 10^4$  can be translated into a limit on time-

<sup>2</sup> The quality factor is defined as the ratio between the energy dissipated during the tidal forcing cycle and the average tidal interaction energy.

lag<sup>3</sup> for the Jupiter-Io interaction  $\tau_{J-I} < 0.062$  s or on the viscous time of  $t_{V,J-I} > 15$  yr (Socrates et al. 2012a).

Note that the constraints on the amount of dissipation in Jupiter (e.g., viscous time) derived from the Jupiter-Io interaction depend only on its internal structure and can, therefore, be used as a benchmark for the tidal interaction between a Jupiter-like planet orbiting its host star.

Recent attempts to calibrate the amount of tidal dissipation using the observed sample of giant planets have been carried out by Hansen (2010, 2012). Hansen (2010) evolves the planetary orbits from an initially prescribed eccentricity-period distribution using the equilibrium tide theory (Hut 1981) (similar to our treatment in Appendix A but ignoring the gravitational interactions due to a perturber) and constraints the amount of dissipation required to fit the data after evolving the systems for 3 Gyr. By fitting the envelope of the observed period-eccentricity distribution the author finds that for Jupiter-like planets the viscous time<sup>4</sup> of the exoplanets should be  $t_V \simeq 230$  yr. Similarly, by studying individual short-period systems with moderate eccentricities Hansen (2010) finds similar values, roughly  $t_V \sim 100 - 1000$  yr, which are consistent similar estimates by Quinn et al. (2014).

Similarly, Socrates et al. (2012a) give a lower limit to the amount of dissipation (an upper limit to the viscous time of the planet  $t_V$ ) required to circularize an initially highly eccentric planetary orbit at  $a \sim 5$  AU to a final circular orbit at  $a \simeq 0.06$  AU within 10 Gyr. Such limit is  $t_V \lesssim 1.5$  yr for a Jupiter-like planet, which is smaller by an order of magnitude than the lower limit  $t_V > 15$  yr inferred from the Jupiter-Io interaction.

The discrepancy found by Socrates et al. (2012a) might not pose a severe problem for high-eccentricity migration given the uncertainties in the models of tidal dissipation and the physical properties of the exoplanets. For instance, this apparent contradiction can be resolved by the recently proposed model by Storch & Lai (2013) in which the dissipation happens in the core of giant planets. In this model, the energy dissipated is a function of the tidal forcing frequency and, depending on the size of the core, the amount of dissipation can match that inferred from Jupiter-Io, while at the same time being orders of magnitude more efficient at longer periods, allowing high-eccentricity migration to operate.

Our approach in this work is to parametrize the amount of tidal dissipation in order to study how it changes the evolution of KL migration and thereby to assess what amount, if any, can best explain the observations.

### 1.5. Plan of this paper

In §2 and §3 we describe the evolution of planetary orbits in two migration regimes: fast and slow KL migration. These sections serve as a basis to understand

<sup>3</sup> The quality factor is related to the viscous time by  $1/Q = 2|\Omega - n|\tau$  where  $\Omega$  is the planet's spin frequency and  $n$  is the mean motion. Similarly, the planets' viscous time  $t_V$  and time-lag  $\tau$  are related by  $t_V = 3(1+k_L)R^3/(Gm\tau)$  where  $k_L$  is the planet's Love number (Eggleton et al. 1998)

<sup>4</sup> The author uses another parametrization in terms of an internal dissipation constant  $\sigma$ , which is related to the viscous time as  $t_V = 2(1+k_L)/(MR^2\sigma)$ .

the results from our Monte Carlo simulations which we present in §4. In §5 and §6 we show the results for the semi-major axis and stellar obliquity distribution of Hot Jupiters from our simulations, which we compare with the observations. In §7, §8, and §9 we characterize the production of Hot Jupiters, intermediate period planets, and non-migrating planets. Finally, in §10 we discuss the implications and limitations from our results and we summarize our main findings in §11.

## 2. SLOW KOZAI-LIDOV MIGRATION

In this section, we study a regime of KL migration that involves multiple KL cycles with the semi-major axis shrinking by a small fractional amount during the high-eccentricity episodes of such cycles. We refer to this migration regime as “slow” KL migration.

The model for orbit evolution used in this section is described in Appendices A and B. In Appendix A, we explicitly show the equations of motion describing the secular evolution of star-planet-star triple system including the effects from general relativistic precession, stellar and planetary spin evolution, and tides. In Appendix B, we provide an analytical expression for the time-averaged eccentricity over a KL cycle in Equations (B6)-(B8).

For the sake of brevity, in some expressions we drop the sub-index “in” when referring to the inner orbit. Thus,  $e \equiv e_{\text{in}}$  and  $a \equiv a_{\text{in}}$ .

### 2.1. Semi-major axis evolution and migration rate

We study the semi-major axis evolution of a slowly migrating planet and calculate its migration rate in the presence of KL cycles.

In the upper panel of Figure 1, we show the semi-major axis and pericenter evolution for migration tracks with different planetary viscous times  $t_{V,2} = 0.1$  yr (red lines) and  $t_{V,2} = 1$  yr (black lines). In both cases, the KL mechanism forces the orbit to a maximum eccentricity of 0.994 and a small pericenter distance of  $a(1-e) \simeq 0.03$  AU. Tides gradually extract orbital energy during the eccentricity maximum of each cycle, so the orbit decays, reaching a final semi-major axis of  $a_F \simeq 0.05$  AU<sup>5</sup>. For the simulation with  $t_{V,2} = 0.1$  yr the planet reaches  $a_F$  after  $\sim 3$  Gyr, while it takes more than 10 Gyr for the simulation with  $t_{V,2} = 1$  yr (the complete evolution is not shown in the figure).

For comparison we include an evolutionary track when there is no perturber and  $t_{V,2} = 1$  yr (green line in Figure 1). Migration proceeds roughly at constant orbital angular momentum because in this example the transfer of angular momentum between the spins and the orbit has little effect on the orbital evolution. The evolution starts from a highly eccentric orbit with  $e = 0.994$ , reaching a pericenter distance of  $a(1-e) = 0.03$  AU, identical (by construction) to the minimum pericenter distance of the simulations undergoing KL cycles described above. In this case, the migration to the final semi-major axis  $a_F = 0.06$  AU takes  $\sim 6$  Gyr. By comparing this track to the one undergoing KL oscillations with  $t_{V,2} = 1$  yr (black solid line), we observe that the former migrates

<sup>5</sup> The minimum pericenter distance decreases from  $a(1-e) \simeq 0.03$  AU to 0.025 AU due to the transfer of orbital angular momentum to the planet's spin that occurs after general relativistic precession quenches the oscillations and migration speeds up.

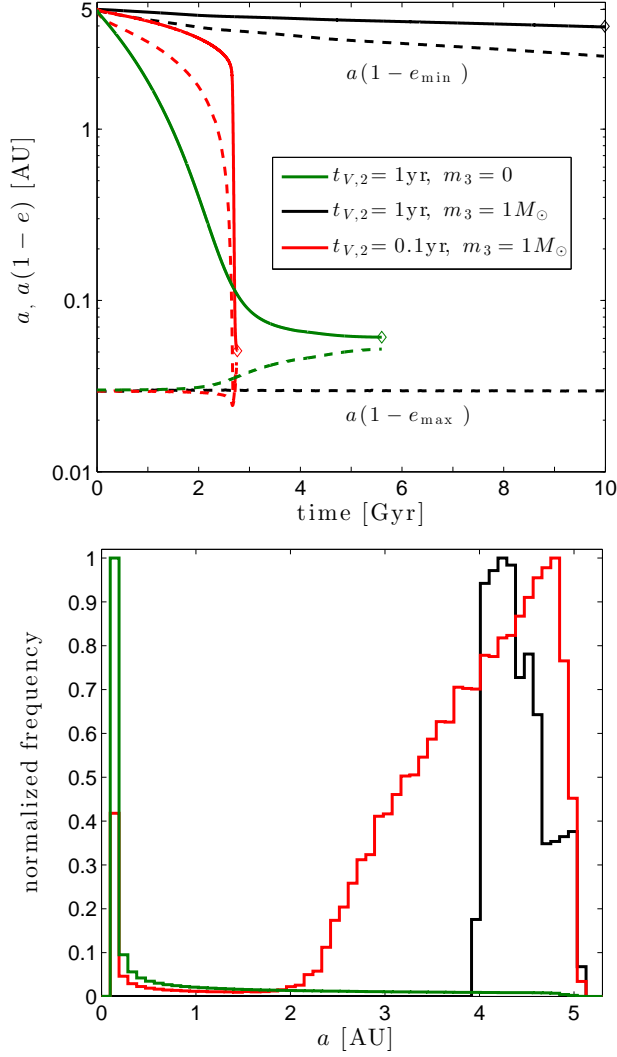


FIG. 1.— Evolution of migrating planets for different planetary viscous times  $t_{V,2}$  and perturber masses  $m_3$  as labeled. *Upper panel:* semi-major axis (solid lines) and pericenter distance (dashed lines). *Lower panel:* time spent in each semi-major axis bin normalized by the tallest bin. The green lines indicate a case in which there is no perturber ( $m_3 = 0$ ) and the planet is initially placed in a highly eccentric orbit with  $a = 5 \text{ AU}$ ,  $e = 0.994$ . The black and red lines indicate the evolution when the perturber has  $m_3 = 1 M_\odot$ ,  $a_{\text{out}} = 500 \text{ AU}$ ,  $e_{\text{out}} = 0$ , and an initial inclination of  $i_{\text{tot}} = 85^\circ.3$  (angle between inner and outer angular orbital momenta), while the planet initially has  $a = 5 \text{ AU}$ ,  $e = 0.01$ ,  $\omega_0 = 0$ ,  $\Omega_0 = 0$ , and a spin period of 20 days (the initial spin period of the host star is set to 10 days). Since these simulations show many KL cycles within a Gyr (initially  $\tau_{\text{KL}} \simeq 2.4 \times 10^6 \text{ yr}$  in Eq. 1) we only display the minimum ( $a[1 - e_{\text{max}}]$ ) and maximum ( $a[1 - e_{\text{min}}]$ ) pericenter distances reached within each KL cycle. All simulations start with zero obliquities (the angles between  $\mathbf{h}_{\text{in}}$  and  $\mathbf{\Omega}_1$  or  $\mathbf{\Omega}_2$ ) and they reach the same minimum pericenter distance  $a(1 - e_{\text{max}}) = 0.03 \text{ AU}$  during migration (the minimum and maximum pericenter distances are the same for the green line). The simulations are stopped once  $a < 0.1 \text{ AU}$  and  $e < 0.1$  or 10 Gyr have passed (the semi-major axis at which the simulation is stopped is indicated with a diamond).

from  $a = 5 \text{ AU}$  to  $\simeq 4 \text{ AU}$  in  $\sim 0.25 \text{ Gyr}$ , while the latter simulation does so in 10 Gyr. Thus, in our example migration proceeds initially  $\sim 40$  times more slowly when the KL oscillations are taken into account.

In the lower panel of Figure 1, we show a histogram

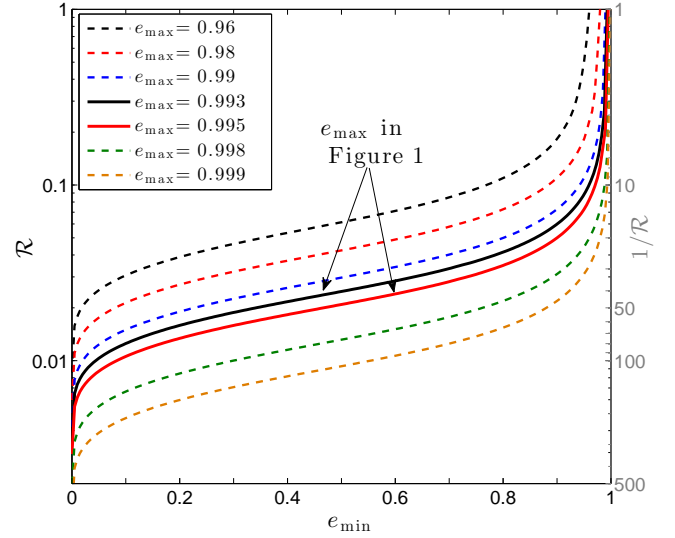


FIG. 2.— Ratio between the migration rate  $|\dot{a}/a|$  averaged over a KL cycle and the migration rate at constant angular momentum ( $\mathcal{R}$  from Eq. 6) as a function of the minimum eccentricity reached in a KL cycle  $e_{\text{min}}$ , for different values of the maximum eccentricity  $e_{\text{max}}$  as labeled. The right y-axis in gray shows the values of the reciprocal  $1/\mathcal{R}$  and the solids curves (red and black) indicate the tracks (range of  $e_{\text{max}}$ ) of our example Figure 1. The migration rate at constant angular momentum is computed at fixed eccentricity  $e_{\text{max}}$ . We assume that all the dissipation occurs inside the planet and that the planet and the star are non-rotating.

of the time spent in each semi-major axis bin (or the time-averaged semi-major axis distribution) during the migration tracks depicted in the upper panel. Note that we stopped the simulations shown by red and green lines once  $a < 0.1 \text{ AU}$  and  $e < 0.1$  so they do not spend an arbitrary amount of time as Hot Jupiters (red and green lines). For the evolution at almost constant angular momentum (green line), the time-averaged semi-major axis distribution follows a power-law  $\propto a^{-1/2}$  during the evolution at high eccentricity, which is expected from the orbit-averaged energy loss rate at fixed periastron distance, which results in  $\dot{a} \propto a^{1/2}$  (Socrates et al. 2012b).

On the contrary, in the simulation with  $t_{V,2} = 0.1 \text{ yr}$  that undergoes KL oscillations (red line) the time-averaged semi-major axis distribution peaks at  $a \sim 4.5 \text{ AU}$  and decays almost linearly from  $a \sim 4.5 \text{ AU}$  to  $a \sim 2 \text{ AU}$ ; for  $a < 1.6 \text{ AU}$  the KL oscillations are damped by general relativistic precession. According to the approximate expression in Equation (3), the oscillations should be completely damped for  $a < 1.1 \text{ AU}$ . Once the oscillations are damped migration proceeds at almost constant angular momentum and the distribution follows the power-law  $\propto a^{-1/2}$ , as expected. In contrast, by increasing the viscous time to  $t_{V,2} = 1 \text{ yr}$  (black line), the time-averaged semi-major axis distribution is restricted to  $a > 4 \text{ AU}$  since the migration timescale to become a Hot Jupiter is longer than 10 Gyr.

We can analytically quantify by how much is migration slowed down by KL oscillations relative to migration at a constant angular momentum (with same minimum pericenter distance or maximum eccentricity  $e_{\text{max}}$ ).

In Appendix B we derive an exact expression for the time-averaged eccentricity distribution  $n_e(e|e_{\text{min}}, e_{\text{max}})$  during a KL cycle in the quadrupole approximation (Equation B8), which depends only on the minimum and

maximum eccentricities reached in a cycle  $e_{\min}$  and  $e_{\max}$ . By assuming that all the dissipation occurs in the planet (i.e., in  $m_2$ ), from Equations (A4)-(A5), (A11)-(A12), and (A16) we can compute the migration rate (inverse of the migration timescale  $\tau_a$ ) as:

$$\tau_a^{-1} = \left| \frac{1}{a} \frac{da}{dt} \right| = \left| 2V_2 \frac{e^2}{1-e^2} + 2W_2 \right| \quad (4)$$

$$\equiv \mathcal{F}(e)/t_{F2}(a), \quad (5)$$

where  $\mathcal{F}(e) \propto (1-e)^{-15/2}$  as  $e \rightarrow 1$ , which reflects the strong dependence of the tidal dissipation rate on the pericenter distance.

Thus, the ratio  $\mathcal{R}$  between the migration rate averaged over a KL cycle and the migration rate at constant angular momentum ( $e = e_{\max}$ ) is

$$\mathcal{R}(e_{\min}, e_{\max}) = \frac{1}{\mathcal{F}(e_{\max})} \int_{e_{\min}}^{e_{\max}} de \mathcal{F}(e) n_e(e|e_{\min}, e_{\max}); \quad (6)$$

note that the dependence on the semi-major axis disappears.

In Figure 2, we show the ratio  $\mathcal{R}$  from Equation (6) as a function of the minimum eccentricity reached in a KL cycle  $e_{\min} \in [0, e_{\max}]$  for different values of the maximum eccentricity  $e_{\max}$ . We observe that  $\mathcal{R} \rightarrow 0$  as  $e_{\min} \rightarrow 0$  because in this limit the eccentricity remains small for an arbitrarily large fraction of the KL cycle. Also,  $\mathcal{R} \rightarrow 1$  when the oscillations are quenched (i.e.,  $e_{\min} \rightarrow e_{\max}$ ), as expected.

From Figure 2, we observe that the ratio  $\mathcal{R}$  decreases as  $e_{\min}$  ( $e_{\max}$ ) decreases (increases). This is because when the eccentricity oscillates with larger amplitude (i.e., smaller  $e_{\min}$  or larger  $e_{\max}$ ) the planet spends a larger fraction of the KL cycle at pericenter distances that are too large for tidal dissipation to occur. Additionally, as we increase  $e_{\max}$  to more extreme values, significant tidal dissipation is constrained to a smaller vicinity around  $e_{\max}$ , so the planetary orbit spends a shorter fraction of the KL cycle dissipating energy.

We can compare our estimates of the migration rate reduction (i.e.,  $\mathcal{R}$  Eq. 6) with our simulations in Figure 1 (black and green lines in the upper panel). As discussed above, the simulations show that migration from  $a = 5$  AU to 4 AU happens  $\sim 40$  times more slowly when KL oscillations are present. Also, the eccentricity reaches a minimum of  $e_{\min} \simeq 0.1 - 0.3$  during the KL cycles at  $a \simeq 4 - 5$  AU. We set  $e_{\max} = 0.993 - 0.995$ , such that for  $a = 5$  AU the minimum pericenter becomes  $a(1 - e_{\max}) = 0.025 - 0.035$  AU, bracketing the value 0.03 AU from the simulation. Thus, from the black and red solid lines in Figure 2 we get  $\mathcal{R} \simeq 0.01 - 0.02$ , meaning that migration with KL oscillations happens  $\sim 50 - 100$  more slowly than that with no oscillations, roughly consistent with the numerical simulation, which results in factor of  $\sim 40$ .

From our numerical example with  $t_{V,2} = 0.1$  yr in Figure 1 (red line), we observe that during migration from  $a = 5$  AU to 2 AU the KL oscillations are gradually damped, while the minimum pericenter distance remains constant. This means that the KL oscillations evolve towards larger values of  $e_{\min}$  and smaller values of  $e_{\max}$  (upward and rightward evolution of  $\mathcal{R}$  in Figure 2). Such evolution increases the value  $\mathcal{R}$  and, therefore,

speeds up the migration relative to that at constant angular momentum, which explains why the time-averaged semi-major axis distribution in the lower panel of Figure 1 decreases as the system migrates from  $a = 5$  AU to 2 AU. For instance, the time-averaged semi-major axis distribution peaks at  $a \simeq 4.5$  AU (red line in lower panel of Figure 1) where the KL oscillations have typically  $e_{\min} \simeq 0.15$ , while it is reduced by a factor of two when  $a \simeq 3.2$  AU where  $e_{\min} \simeq 0.55$ . This is consistent with the results for  $\mathcal{R}$  in Figure 2, where we observe that an evolution from  $e_{\min} = 0.15$  to  $e_{\min} = 0.55$  increases  $\mathcal{R}$  by a factor of  $\simeq 2$  when  $e_{\max} = 0.993 - 0.995$  (black and red solid lines).

In summary, our numerical example and analytical calculations show that KL oscillations typically slow down the migration by  $\sim 2$  orders of magnitude relative to migration at constant angular momentum. This implies that a migrating planet spends most of its life either at a few AU undergoing KL oscillations or as a Hot Jupiter (i.e.,  $a < 0.1$  AU). Thus, migration at a few AU becomes the “bottleneck” that limits the ability of slow migration to produce Hot Jupiters. Once the KL cycles are quenched, migration occurs much faster.

## 2.2. Condition for slow migration

Slow migration occurs only if the secular torque from the companion is strong enough that it can change periastron distance before tidal dissipation is able to shrink the semi-major axis significantly.

From Equations (A4)-(A5), the characteristic timescale in which the secular torque changes the periastron distance  $r_p = a(1 - e)$  in the limit  $1 - e \ll 1$  is

$$\tau_p \equiv \left| \frac{1}{r_p} \frac{dr_p}{dt} \right|^{-1} \simeq \frac{(1 - e^2)\tau_{\text{KL}}}{5|(\hat{\mathbf{q}}_{\text{in}} \cdot \hat{\mathbf{h}}_{\text{out}})(\hat{\mathbf{e}}_{\text{in}} \cdot \hat{\mathbf{h}}_{\text{out}})|}, \quad (7)$$

where the denominator is of order unity during an eccentricity maximum of the KL cycle<sup>6</sup> and  $\tau_{\text{KL}}$  is the KL timescale given in Equation (1).

There is a critical pericenter distance  $r_{p,c}$  at which the migration timescale  $\tau_a$  in Equation (5) equals  $\tau_p$  in Equation (7). By assuming that all the dissipation happens inside the planet and that the planet is non-rotating ( $\Omega_2 = 0$ ), we get

$$r_{p,c} \simeq 0.005 \text{ AU} \left[ \left( \frac{m_1}{M_\odot} \right)^{2.5} \left( \frac{M_J}{m_2} \right)^2 \left( \frac{0.1 \text{ yr}}{t_{V,2}} \right) \left( \frac{R_2}{R_J} \right)^8 \left( \frac{5 \text{ AU}}{a} \right)^3 \left( \frac{a_{\text{out}} \sqrt{1 - e_{\text{out}}^2}}{100 \text{ AU}} \right)^3 \left( \frac{M_\odot}{m_3} \right) \right]^{1/6.5}. \quad (8)$$

Clearly, slow migration requires that  $\tau_a \gg \tau_p$ , which implies that during the KL cycles the planetary orbit has to avoid pericenters distances that are too close to  $r_{p,c}$ . Given the strong dependence of tidal dissipation on the pericenter distance, keeping the pericenter distance

<sup>6</sup> At maximum eccentricity the inclination is minimum and it roughly corresponds to the critical inclination for KL oscillations:  $|\cos(i_{\text{tot}})| = \hat{\mathbf{h}}_{\text{in}} \cdot \hat{\mathbf{h}}_{\text{out}} \simeq \sqrt{3/5}$ , implying that  $(\hat{\mathbf{q}}_{\text{in}} \cdot \hat{\mathbf{h}}_{\text{out}})^2 + (\hat{\mathbf{e}}_{\text{in}} \cdot \hat{\mathbf{h}}_{\text{out}})^2 \simeq 2/5$ .

$a(1 - e) > 2r_{p,c}$  might be enough to meet the condition for slow migration.

From our example in Figure 1, we observe that the minimum pericenter in the black and red lines is  $a(1 - e) = 0.03$  AU, while from Equation (8) we get  $r_{p,c} = 0.0074$  AU and  $r_{p,c} = 0.0105$  AU, respectively. Thus, our example is well outside the critical pericenter and is in the slow migration regime, as expected from the evolution depicted in the figure.

### 2.3. Constraints on tidal dissipation

In this subsection, we constrain the minimum level of dissipation required to form a Hot Jupiter within the lifetime of the planetary system. This approach is similar in principle to the calculation in Socrates et al. (2012a), but considering the presence of KL cycles.

We have shown that the “bottleneck” that limits the production of Hot Jupiters during migration is the phase in which the planetary orbit is undergoing KL oscillations. This allows us to give an approximate condition for KL migration to occur: the migration timescale  $\tau_a = |a/\dot{a}|$  of a planet at a few AU undergoing KL oscillations has to be less than  $\sim 10$  Gyr. From Equations (5) and (6), taking the limit  $1 - e_{\max} \ll 1$ , we can write the time-averaged migration timescale over a KL cycle as

$$\langle \tau_a \rangle_{\text{KL}} \simeq \frac{2^{25/2} t_{F,2}(a) (1 - e_{\max})^{15/2}}{3861 \mathcal{R}(e_{\min}, e_{\max})}. \quad (9)$$

If migration proceeds slowly and at constant minimum angular momentum ( $\propto [a(1 - e_{\max}^2)]^{1/2}$ ) down to the final semi-major axis  $a_F = a(1 - e_{\max}^2)$ , we get the following condition for slow KL migration:

$$\begin{aligned} \frac{\langle \tau_a \rangle_{\text{KL}}}{10 \text{ Gyr}} &\simeq \left( \frac{t_{V,2}}{0.4 \text{ yr}} \right) \left( \frac{0.01}{\mathcal{R}} \right) \left( \frac{a_F}{0.06 \text{ AU}} \right)^{15/2} \left( \frac{a}{5 \text{ AU}} \right)^{1/2} \\ &\times \left( \frac{m_2}{M_J} \right)^2 \left( \frac{M_\odot}{m_1} \right)^2 \left( \frac{R_J}{R_2} \right)^8 < 1, \end{aligned} \quad (10)$$

where  $\mathcal{R}$  in Equation (6) contains the details of the KL oscillations (see Figure 2 for reference).

For the fiducial parameters in Equation (10), we constrain the amount of tidal dissipation to  $t_{V,2} < 0.4$  yr, while for similar parameters Socrates et al. (2012a) find that migration from 5 AU to  $\simeq 0.06$  AU at constant angular momentum requires  $t_{V,2} < 1.5$  yr. Thus, our constraint is  $\sim 4$  times more stringent than that in Socrates et al. (2012a). Note that the bottleneck in Socrates et al. (2012a) is the migration at  $a \lesssim 1$  AU since the migration at constant angular momentum is much slower for  $a \sim 0.06 - 1$  AU than for  $a \sim 1 - 5$  AU (see green line in Figure 1). In contrast, the migration timescale with KL cycles is determined by that at  $a \gtrsim 1$  AU, where the planet is undergoing KL oscillations. Therefore, we do not expect to recover the condition by Socrates et al. (2012a) by just suppressing the KL cycles (i.e., setting  $\mathcal{R} = 1$ ) in Equation (10).

As an example, we can apply the constraint in Equation (10) to the hypothetical evolutionary track of HD 80606b depicted by Fabrycky & Tremaine (2007) (Figure 1 therein) in which the authors use stellar and planetary masses of  $m_1 = 1.1M_\odot$  and  $m_2 = 7.8M_J$ . The planet

migrates from  $a = 5$  AU to a final semi-major axis of  $a_F = 0.071$  AU. Thus, Equation (10) yields  $t_{V,2} < 0.0023$  yr, consistent with the value used by the authors of  $t_{V,2} = 0.001$  yr.

We have limited our analysis to the case in which the secular gravitational interaction is approximated up to the quadrupole level in  $a_{\text{in}}/a_{\text{out}}$  ( $\epsilon_{\text{oct}} = 0$  in Eq. A3), which is valid when  $a_{\text{in}} \ll (1 - e_{\text{out}})a_{\text{out}}$ . Stellar binaries have a wide eccentricity and, therefore, our approximation might break down in some cases. We still expect that our constraint on the amount of dissipation remains valid because the eccentricity modulation from the octupole happens on timescales that are longer than the KL timescale (Katz, Dong, & Malhotra 2011; Naoz et al. 2012). Thus, this longer-timescale eccentricity modulation would make the planet spend a larger fraction of a KL cycle at pericenter distances that are too large for tidal dissipation to occur, slowing down migration even longer compared to the quadrupole-level estimates. We study the effect of the octupole and the other relevant forces using Monte Carlo simulations in §4.

### 3. FAST KOZAI-LIDOV MIGRATION

In this section, we study the regime of KL migration in which tidal dissipation is strong enough that the semi-major axis shrinks significantly before the secular torque from the companion has time to change the periastron distance. We refer to this migration regime as “fast” KL migration.

We expect that fast KL migration occurs roughly when the migration timescale ( $\tau_a$  in Eq. [5]) equals the timescale for the secular torque to change the periastron distance significantly ( $\tau_p$  in Eq. [7]). We showed in §2.2 that both timescales are equal at a critical pericenter distance  $r_{p,c}$  given by Equation (8). Once this critical pericenter is reached, migration occurs at roughly constant angular momentum, so the final semi-major axis becomes  $a_F \simeq 2r_{p,c}$ . Thus, by assuming that all the dissipation happens inside the planet and that the planet is non-rotating ( $\Omega_2 = 0$ ), we get

$$\begin{aligned} a_F &\simeq 0.012 \text{ AU} \left[ \left( \frac{m_1}{M_\odot} \right)^{2.5} \left( \frac{M_J}{m_2} \right)^2 \left( \frac{0.1 \text{ yr}}{t_{V,2}} \right) \left( \frac{R_2}{R_J} \right)^8 \right. \\ &\quad \left. \left( \frac{5 \text{ AU}}{a} \right)^3 \left( \frac{a_{\text{out}} \sqrt{1 - e_{\text{out}}^2}}{100 \text{ AU}} \right)^3 \left( \frac{M_\odot}{m_3} \right) \right]^{1/6.5}, \end{aligned} \quad (11)$$

where we have slightly changed the pre-factor from 0.01 AU that results from  $a_F \simeq 2r_{p,c}$  (Eq. [8]) to 0.012 AU to better reproduce the results from a set of numerical simulations with fast-migrating planets.

A similar expression for  $a_F$  in Equation (11) is found by Wu et al. (2007) by equating the eccentricity forcing to the eccentricity damping due to tides.

Fast KL migration is expected to be the source of the shortest-period Hot Jupiters and these are particularly susceptible to collisions with the star or tidal disruption. Note that for the fiducial parameters in Equation (8) we have a critical pericenter distance  $r_{p,c} \simeq R_\odot$ , meaning that the planet can collide before tides become strong enough to shrink the semi-major axis significantly. Moreover, planets that approach the star too closely can be tidally disrupted at even larger separations

of  $\sim 2 - 3R_\odot$  (Guillochon et al. 2011; Liu et al. 2012). Thus, one might expect that an important fraction of the fast migrating planets are likely to be destroyed. We show in §4 by means of Monte Carlo simulations that this is indeed the case.

We note that  $a_F$  in Equation (11) depends strongly on the radius of the planet, as  $a_F \propto R_2^{8/6.5}$ . Interestingly, gaseous giant planets are expected to form with an initially larger radii, which is then shrunk as the planet cools down. This suggests that radius shrinkage of fast-migrating planets can shift  $a_F$  to larger values (Wu et al. 2007). Note, however, that by increasing the planetary radii the distance at which the planet is tidally disrupted also increases and the effect of time-varying radius on the migration track is far from clear. In §5.3, we test the effect of radius shrinkage on our simulations.

#### 4. NUMERICAL EXPERIMENTS

We run numerical experiments for the evolution of triple systems consisting of a wide stellar binary with masses  $m_1 = 1M_\odot$  and  $m_3$  and a planet orbiting  $m_1$  with mass  $m_2 = 1M_J$ . The radii are taken to be solar for the host star and in most simulations the planet has a Jupiter radius (see Table 1). The equations of motion are fully described in Appendix A.

##### 4.1. Initial conditions

The relative initial inclination of the orbits is drawn from an isotropic distribution, i.e.,  $\cos(i_{\text{tot}}) = \hat{\mathbf{h}}_{\text{in}} \cdot \hat{\mathbf{h}}_{\text{out}}$  uniformly distributed in  $[-1, 1]$ . The longitude of the argument of pericenter and longitude of the ascending node are chosen randomly for the inner and outer orbits. The planets start at a fixed semi-major axes of 5 AU with an eccentricity that follows a Rayleigh distribution:

$$dp = \frac{e}{\sigma_e^2} \exp\left(-\frac{1}{2}e^2/\sigma_e^2\right), \quad (12)$$

where  $\sigma_e$  is an input parameter chosen to be 0.01 in most simulations.

The semi-major axes of the stellar binaries is chosen to be uniform in  $\log(a_{\text{out}})$ , motivated by the observed binary period distributions at semi-major axis  $>100$  AU (e.g., Duquennoy & Mayor 1991; Raghavan et al. 2010). We consider a semi-major axis in the range of 100-1500 AU. The binary eccentricity is taken to be uniformly distributed in  $e_{\text{out}}^2$  (constant phase-space density at fixed orbital energy). We impose a maximum binary eccentricity of 0.9 in most simulations. We also run one simulation (Ecc-tv01 in Table 1) with a uniform distribution in  $e_{\text{out}}$ , motivated by the distribution observed in solar-type stars by Raghavan et al. (2010). We discard systems that do not satisfy the stability condition (Mardling & Aarseth 2001):

$$\frac{a_{\text{out}}}{a_{\text{in}}} > 2.8(1 + \mu)^{2/5} \frac{(1 + e_{\text{out}})^{2/5}}{(1 - e_{\text{out}})^{6/5}} \left(1 - 0.3 \frac{i_{\text{tot}}}{180^\circ}\right) \quad (13)$$

where  $\mu = m_3/(m_1 + m_2)$ .

The host star and the planet start spinning with periods of 10 days (expect for Spin-tv0.1) and 10 hours, respectively, both along the  $\hat{\mathbf{h}}_{\text{in},0}$  axis, implying that the initial obliquities (the angles between  $\hat{\mathbf{h}}_{\text{in}}$  and  $\boldsymbol{\Omega}_1$  or  $\boldsymbol{\Omega}_2$ ), are zero.

##### 4.2. Stopping conditions

We stop our simulations when at least one of the following conditions happens:

1. A maximum time has passed. We choose this maximum time uniformly distributed between 0 and 10 Gyr, which is meant to provide a final sample of planetary systems as it would be observed if the rate of star formation is constant.
2. A Hot Jupiter in a circular orbit is formed: the planetary orbit reaches  $a < 0.1$  AU and  $e < 0.01$ . Following these systems for a long times is computationally expensive and a significant evolution is mostly seen in the eccentricity, which decreases to even lower values (see, however, the discussion in §10.2.1 about tidal dissipation in the host star).
3. The planet is tidally disrupted. Disruption can happen when the planet reaches small pericenter distances. Hydrodynamic simulations for Jupiter-like planets (Faber et al. 2005; Guillochon et al. 2011; Liu et al. 2012) show that the pericenter distance at which a planet in a highly eccentric orbit gets disrupted<sup>7</sup> is

$$R_t = f_t R_p \left( \frac{m_1}{m_1 + m_2} \right)^{-1/3}, \quad (14)$$

where the dimensionless coefficient  $f_t$  is of order unity. The simulations by Guillochon et al. (2011) and Liu et al. (2012) result in  $f_t = 2.7$ , and, as argued by these authors, this value might be regarded as a lower limit since disruptions at wider separations might still happen over timescales longer than in their simulations. Similar simulations by Faber et al. (2005) report a disruption distance that is slightly smaller:  $f_t = 2.16$ . However, Naoz et al. (2012) have carried Monte Carlo simulations similar to the ones we present here, but have used a different and much less restrictive disruption distance:  $f_t = 1.66$ .

In order to study how the results depend on the disruption criterion we decided to stop most simulations only when the planet collides with star (i.e.,  $a(1 - e) < R_1 + R_2$ ) and record the time whenever a new minimum pericenter is reached. For the simulations Rp-tv0.1 and Rp-tv0.01 where the radius of the planet varies in time we use the disruption criterion as  $f_t = 2.7$  in Equation (14), while in Rp-tv0.03 we use  $f_t = 3.2$ .

Note that all simulations (except for MC-tv0.1-td and Rp-tv0.03) use  $f_t = 2.7$  in Equation (14) to classify a system as tidally disrupted.

##### 4.3. Results

We classify the outcomes from our simulations into four categories;

<sup>7</sup> Depending on the orbital eccentricity, the planet can be either ejected after substantial mass loss or completely disrupted (Guillochon et al. 2011). We refer to both outcomes as tidal disruptions.

TABLE 1  
SUMMARY OF SIMULATED SYSTEMS AND OUTCOMES

| Name                     | $a_{\text{out}}$ [AU] | $m_3$ [ $M_\odot$ ] | $f(e_{\text{out}})$            | $R_p$ [ $R_J$ ]                                   | $t_{V,2}$ [yr] | $N_{\text{sys}}$ | HJ (%) | Mig. (%) | TD (%) | Non-Mig. (%) |
|--------------------------|-----------------------|---------------------|--------------------------------|---|----------------|------------------|--------|----------|--------|--------------|
| MC-tv0.1                 | 100 – 1500            | 1                   | $U(e_{\text{out}}^2; 0, 0.81)$ | 1   | 0.1            | 6009             | 3.4    | 0.3      | 25.0   | 71.3         |
| MC-tv0.1-nt <sup>a</sup> | 100 – 1500            | 1                   | $U(e_{\text{out}}^2; 0, 0.81)$ | 1   | 0.1            | 6009             | 26.1   | 0.3      | 2.3    | 71.3         |
| MC-tv1                   | 100 – 1500            | 1                   | $U(e_{\text{out}}^2; 0, 0.81)$ | 1   | 1              | 4052             | 1.5    | 0.1      | 26.1   | 72.3         |
| MC-tv0.01                | 100 – 1500            | 1                   | $U(e_{\text{out}}^2; 0, 0.81)$ | 1   | 0.01           | 4095             | 7.4    | 0.3      | 21.7   | 70.6         |
| Ecc-tv0.1                | 100 – 1500            | 1                   | $U(e_{\text{out}}; 0, 0.95)$   | 1   | 0.1            | 4235             | 3.2    | 0.4      | 19.2   | 77.2         |
| Mass-tv0.1               | 100 – 1500            | 0.1                 | $U(e_{\text{out}}^2; 0, 0.81)$ | 1   | 0.1            | 3912             | 5.0    | 0.2      | 19.5   | 75.3         |
| Spin-tv0.1 <sup>b</sup>  | 100 – 1500            | 1                   | $U(e_{\text{out}}^2; 0, 0.81)$ | 1   | 0.1            | 5824             | 3.4    | 0.3      | 28.1   | 68.2         |
| Rp-tv0.1                 | 100 – 1500            | 1                   | $U(e_{\text{out}}^2; 0, 0.81)$ | $1 + e^{-t/(3 \cdot 10^7 \text{ yr})}$            | 0.1            | 5212             | 2.4    | 0.9      | 21.4   | 75.3         |
| Rp-tv0.01                | 100 – 1500            | 1                   | $U(e_{\text{out}}^2; 0, 0.81)$ | $1 + e^{-t/(3 \cdot 10^7 \text{ yr})}$            | 0.01           | 4213             | 6.2    | 1.1      | 19.4   | 73.3         |
| Rp-tv0.03 <sup>c</sup>   | 100 – 1500            | 1                   | $U(e_{\text{out}}^2; 0, 0.81)$ | $1 + \frac{1}{2}e^{-t/(3 \cdot 10^7 \text{ yr})}$ | 0.03           | 5485             | 2.3    | 0.7      | 25.7   | 71.3         |
| SMA500e0                 | 500                   | 1                   | $e_{\text{out}} = 0$           | 1   | 0.01           | 7070             | 10.2   | 1.5      | 0      | 88.3         |

Note: all simulations have  $m_1 = M_\odot$ ,  $m_2 = M_J$ , and  $t_{V,1} = 50$  yr.  $U(x; x_{\text{min}}, x_{\text{max}})$  is the uniform distribution with  $x_{\text{min}} < x < x_{\text{max}}$ .

We classify the outcomes as: *Hot Jupiters* (HJ) ( $a < 0.1$  AU), *Migrating* (Mig.) ( $0.1 \text{ AU} < a < 4.5$  AU), *Tidally Disrupted* (TD) (Mig.) (minimum pericenter  $< R_t$  with  $R_t$  given by Eq. [14] with  $f_t = 2.7$ ), *Non-Migrating* (Non-Mig.) ( $a > 4.5$  AU).

(<sup>a</sup>) MC-tv0.1-nt is identical to MC-tv0.1, but assuming that planets are only disrupted by collisions with the star, i.e.,  $R_t = R_\odot + R_J$  in Equation (14).

(<sup>b</sup>) In Spin-tv0.1 identical to MC-tv0.1, but we change the initial host star's spin period from 10 days to 3 days.

(<sup>c</sup>) In Rp-tv0.03, we set  $f_t = 3.2$  in Eq. [14].

1. systems that form a *Hot Jupiter* (HJ), defined as those that migrate to  $a < 0.1$  AU;
2. systems with *migrating* (Mig.) planets, defined as those with  $0.1 \text{ AU} < a < 4.5$  AU at the end of the simulation;
3. systems with *tidally disrupted* (TD) planets, defined as those that reach pericenters smaller than  $R_t$  with  $f_t = 2.7$  in Equation (14);
4. systems with *non-migrating* (Non-Mig.) planets, defined as those with  $a > 4.5$  AU at the end of the simulation.

In Table 1, we show the parameters of our simulations and the branching ratios into each category of outcome. We choose MC-tv0.1 as our fiducial simulation and discuss this first, then compare it with the rest of the simulations.

From Table 1 and Figure 3, we observe that the most common outcome in MC-tv0.1 is systems with non-migrating planets (black dots,  $\simeq 71\%$ ). From panel (b) in Figure 3, this outcome is preferentially found in systems in which the outer companion has relatively low inclination and eccentricity, so the KL mechanism<sup>8</sup> does not produce high enough eccentricities for efficient tidal dissipation to occur. Also, non-migrating systems are slightly more common when the stellar perturbers are more widely spaced: the median of the outer semi-major axis is  $\simeq 515$  AU compared to  $\simeq 410$  AU for all the systems. This might be because the KL timescale increases as  $\propto a_{\text{out}}^3$  (Eq. [1]), which allows for the extra forces that cause apsidal precession (e.g., general relativity) to limit the eccentricity growth more easily for more distant companions.

From panel (a) in Figure 3, we observe that some systems have migrated outwards by  $\lesssim 10\%$  (black dots with final  $a > 5$  AU) as a result of the angular momentum

<sup>8</sup> The critical mutual inclination for KL oscillations to occur is given by  $|\cos(i_{\text{tot}})| \leq \sqrt{3/5} \simeq 0.78$  or  $i_{\text{tot}} \in [39.2^\circ, 140.8^\circ]$ .

transferred from the planet's spin to a highly eccentric planetary orbit during the simulation.

The second most common outcome is tidal disruptions (blue circles,  $\simeq 25\%$ ), in systems where the planetary orbit becomes extremely eccentric reaching  $a(1 - e) < 0.0127$  AU (i.e.,  $R_t$  with  $f_t = 2.7$  in Eq. [14]). In §3 we argued that disruptions happen only if the timescale at which the KL mechanism changes the pericenter distance is shorter than the migration timescale. From Equation (8) the condition above translates into  $r_{p,c} < a(1 - e)$ , where  $r_{p,c}$  is the critical pericenter at which both timescales are equal. Thus, a necessary condition for disruptions is  $r_{p,c} < R_t$ , which for the parameters in our fiducial simulation constrains the perturber to

$$a_{\text{out}} \sqrt{1 - e_{\text{out}}^2} < 750 \text{ AU}, \quad (15)$$

which is satisfied by all the systems with disrupted planets (see dashed line and blue points in panel d of Figure 3). Thus, the disrupted systems are preferentially found in more eccentric and tighter binaries (panel d): the median  $e_{\text{out}}$  ( $a_{\text{out}}$ ) in disrupted systems is  $\simeq 0.72$  ( $\simeq 225$  AU) compared to  $\simeq 0.62$  ( $\simeq 410$  AU) for the whole sample. Note also that for more eccentric and tighter perturbers the octupole-level gravitational perturbations ( $\epsilon_{\text{oct}}$  in Eq. [A3]) become stronger, allowing for more phase-space volume at which the planets can reach very high eccentricities (Naoz et al. 2011; Katz, Dong, & Malhotra 2011). For instance, from panel (d) we observe that the distribution of the initial mutual inclinations in disrupted systems widens as we increase  $e_{\text{out}}$ , reaching  $i_{\text{tot}} \sim 50^\circ - 130^\circ$  for  $e_{\text{out}} > 0.6$ .

From panel (c) in Figure 3, we observe that most planets get tidally disrupted early on in the simulation and some of them migrated inwards by as much as 3 AU before crossing the tidal disruption radius. From Equation (10) we can estimate the shortest migration timescale by setting  $a_F = 2R_t = 0.0254$  AU, which results in  $\langle \tau_a \rangle_{\text{KL}} \sim 6 \cdot 10^6$  yr. This is consistent with the simulation where all the planets that migrate to  $a < 4$  AU before being disrupted have evolved for  $> 10^7$  yr (panel

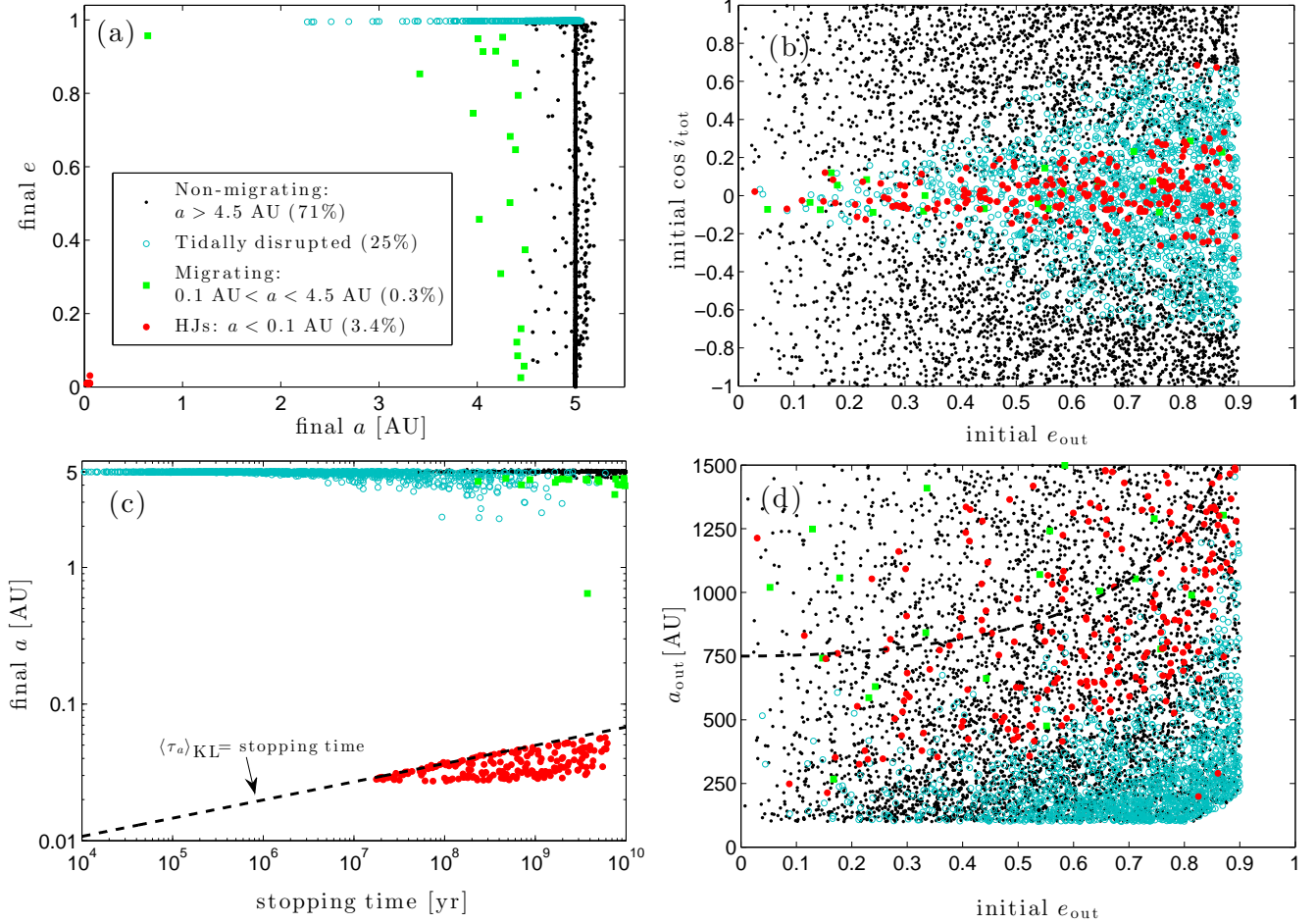


FIG. 3.— Outcomes for the fiducial Monte Carlo simulation MC-tv0.1 (see Table 1), as labeled in panel (a). The stellar binary has a uniform distribution in  $\log(a_{\text{out}})$  in  $[100, 1500]$  AU and an eccentricity distribution that is uniform in  $e_{\text{out}}^2$  in  $[0, 0.81]$ . We set the stellar and planetary viscous times to  $t_{V,1} = 50$  yr and  $t_{V,2} = 0.1$  yr, respectively. The planetary orbits are initialized with  $a = 5$  AU and their eccentricities are drawn from the distribution in Equation (12) with  $\sigma_e = 0.01$ , corresponding to nearly circular orbits. The planets are labeled as disrupted (blue circles) if the pericenter becomes smaller than  $0.0127$  AU ( $R_t$  with  $f_t = 2.7$  in Eq. [14]). Panel (a): final semi-major axis versus final eccentricity of the planetary orbit. Panel (b): initial eccentricity of the stellar binary  $e_{\text{out}}$  versus initial cosine of inclination of the inner and outer orbits (angle between the orbital angular momentum vectors). Panel (c): time at which the simulation is stopped versus the final semi-major axis. The dashed line indicates the boundary at which  $\langle \tau_a \rangle_{\text{KL}}$  in Equation (10) equals the stopping time. Panel (d): initial eccentricity of the stellar binary  $e_{\text{out}}$  versus the semi-major axis of the stellar binary. The dashed line indicates the boundary  $a_{\text{out}}(1 - e_{\text{out}}^2)^{1/2} = 750$  AU (Eq. 15) for tidal disruptions.

c).

The third most common outcome is the systems that form a Hot Jupiter (red dots,  $\simeq 3.4\%$ ). Compared to the systems that have disruptions, almost all ( $\simeq 99\%$ ) of the HJs are formed in systems with an initially narrow range of mutual inclinations:  $|i_{\text{tot}} - 90^\circ| < 20^\circ$  (panel b), and larger semi-major axis of the perturber: mean and median  $a_{\text{out}}$  of 890 AU and 845 AU (panel d). These observations might be linked because for more distant perturbers the contribution from the octupole-level gravitational interactions becomes weaker and more easily quenched by general relativistic precession (Naoz et al. 2013b), implying that the initial mutual inclinations need to be closer to  $90^\circ$  for the quadrupole-level interactions can force the orbit to very high eccentricities. Additionally, planets reaching very high eccentricities in systems with weaker perturbers (i.e., larger values of  $a_{\text{out}}(1 - e_{\text{out}}^2)^{1/2}$ ) are less likely to be disrupted (Eq. [10]), and can instead form HJs.

All of the HJs are formed after  $\sim 10^7$  yr as required for the minimum migration timescale of  $\sim 6 \cdot 10^6$  yr, discussed above. As seen in panel (c) of Figure 3, HJs with larger final semi-major axis are formed later in an average sense, as expected. We show the boundary at which  $\langle \tau_a \rangle_{\text{KL}}$  in Equation (10) equals the stopping time (i.e., time it takes to form a HJ). Recall that  $\langle \tau_a \rangle_{\text{KL}}$  is the minimum timescale for a planet undergoing slow KL migration to reach a final semi-major axis  $a_F$  and, therefore, at fixed  $a_F$  we expect HJs to be formed in longer timescales (i.e., below this boundary), which is consistent with the simulations.

The least common outcome is the systems with migrating planets ( $\simeq 0.3\%$ ). These systems require that their migration timescale is slightly longer than their actual ages (or stopping time in our simulations). From panel (c), we see that there is only one planet in the migration track  $a(1 - e^2) \sim 0.05$  AU (system with  $a = 0.65$  AU and  $e = 0.96$ ), while the rest have  $a(1 - e^2) > 0.4$

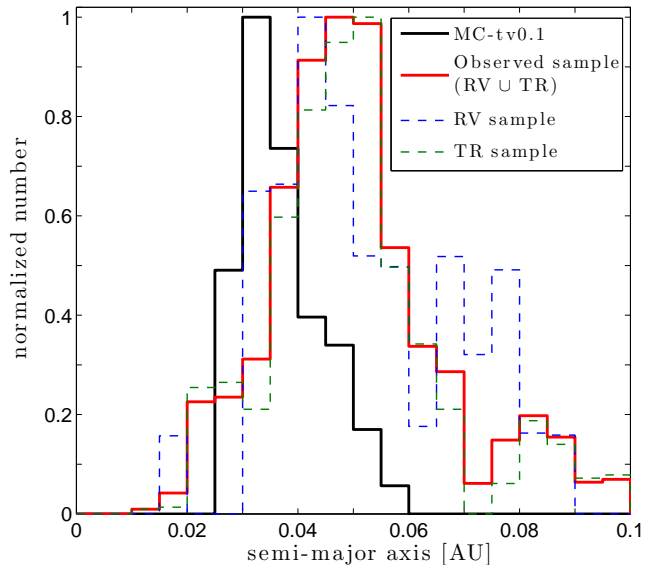


FIG. 4.— Semi-major axis distribution for the Hot Jupiters formed in the fiducial simulation MC-tv0.1 (solid black line) and the observed sample of planets with  $M \sin(i) > 0.1M_J$  and  $a < 0.1$  AU detected in radial velocity (dashed blue line) and transit (green dashed line) surveys, and the combination of both observed samples (solid red line). We correct the transit sample by the geometric selection bias. All histograms are normalized by the tallest bin. The bin width is 0.005 AU.

AU and are, therefore, off the migration track undergoing KL oscillations. For reference, the typical migrating planet has a companion with  $a_{\text{out}}(1 - e_{\text{out}})^{1/2} \sim 500$  AU for which  $\tau_{\text{KL}}$  in Equation (1) becomes equal to the GR precession timescale at  $a \sim 1.5$  AU and the oscillations would be quenched completely for smaller  $a$ . Recall from §2.1 that once the KL oscillations are quenched, migration proceeds much faster (a factor of  $\sim 50 - 100$ ) and, therefore, almost no migrating planets are expected at  $a < 1.5$  AU, consistent with the simulations. The small number of migrating planets is striking and will be further discussed in §8.

##### 5. SEMI-MAJOR AXIS DISTRIBUTION OF HOT JUPITERS

As of January 2013, the observed sample of Hot Jupiters<sup>9</sup> (planets with  $M \sin(i) > 0.1M_J$  and  $a < 0.1$  AU) contains 196 planets, 159 planets detected in transit (TR) and 37 detected by radial velocity (RV) surveys. The former sample has a mean (median) semi-major axis of 0.045 AU (0.045 AU), while the latter sample has a mean semi-major axis of 0.052 AU (0.048 AU). After accounting for the geometric selection bias<sup>10</sup> for the planets detected in transit surveys, the mean (median) semi-major axis is 0.050 AU (0.049). In contrast, RV surveys generally have uniform sensitivity in the semi-major axis

<sup>9</sup> Taken from The Exoplanet Orbit Database (Wright et al. 2011).

<sup>10</sup> Extra selection biases might affect the derived semi-major axis distribution for the transit planets. For instance, by accounting for the detection probability for a given S/N, Gaudi et al. (2005) find a detection efficiency  $\propto a^{-5/2}$ , which yields a mean (median) semi-major axis of 0.057 AU (0.052 AU) in our sample of planets detected in transit surveys. We ignore this extra correction to the semi-major axis distribution in this section, but use it in §7.1. Note that a semi-major axis distribution skewed to larger values would strengthen the main result of this section: KL migration generally produces semi-major axes that are smaller than those observed.

range of our sample and selection effects should not affect the semi-major distribution significantly (Butler et al. 2006; Cumming et al. 2008).

Strictly speaking, our results should be compared with the HJ systems with detected binary companions. However, such sample is too small (16 systems) to make a statistical comparison with our results and the sample of detected binary companions is likely to be fairly incomplete. Thus, we ignore whether a HJ in our sample has a detected binary companion or not. We note, however, that our conclusions might not differ significantly by considering the sample of HJ systems with detected stellar companions since their mean and median semi-major axes is  $\sim 0.048$  AU, roughly consistent with our much larger sample of all HJ systems.

A Kolmogorov-Smirnov (KS) test between the RV and TR semi-major axis distributions shows that these distributions are consistent ( $p$ -value  $\simeq 0.4$ ). Based on these findings, we combine the sample from TR (corrected by the geometric selection bias) and RV surveys, which leaves a sample of 196 planets with mean (median) semi-major axis of 0.050 AU (0.049 AU). We use this distribution for our subsequent analysis.

A useful measure for subsequent analysis is the ratio between the number of Very Hot Jupiters (VHJs,  $a < 0.04$  AU or orbital periods  $< 3$  days) and the total number of Hot Jupiters ( $a < 0.1$  AU):

$$\mathcal{F}_{\text{VHJ}} = \frac{\#\{a < 0.04 \text{ AU}\}}{\#\{a < 0.1 \text{ AU}\}}. \quad (16)$$

The RV (TR) sample has  $\mathcal{F}_{\text{VHJ}} \simeq 0.25$  ( $\mathcal{F}_{\text{VHJ}} \simeq 0.24$ ), while the combined sample has  $\mathcal{F}_{\text{VHJ}} \simeq 0.24$ . Similarly, by combining RV and TR samples Gaudi et al. (2005) find that the ratio between the number of HJs with  $a \simeq 0.02 - 0.04$  AU and the number of HJs with  $a \simeq 0.04 - 0.085$  AU is  $\sim 0.1 - 0.2$ , which roughly translates into  $\mathcal{F}_{\text{VHJ}} \sim 0.09 - 0.17$ . Similarly, Gould et al. (2006) find that the ratio between the number of HJs with  $a \simeq 0.02 - 0.04$  AU and the number of HJs with  $a \simeq 0.04 - 0.06$  AU is  $\simeq 0.45$  (i.e.,  $\mathcal{F}_{\text{VHJ}} \lesssim 0.3$ ).

In Figure 4 we show the semi-major axis distribution for the HJs formed in MC-tv0.1 (black line) and that from the observed sample (red dashed line). The former distribution has a semi-major axis range  $\simeq 0.025 - 0.06$  AU and is highly skewed towards low values: median of 0.034 AU and  $\mathcal{F}_{\text{VHJ}} \simeq 0.75$  (compared to  $\simeq 0.24$  in the observed sample). The peak at  $\sim 0.03$  AU is set by the disruption boundary, which implies that HJs are constrained to have a minimum semi-major axis  $> 2R_t \simeq 0.025$  AU (Eq. 14). This suggests that by having a less restrictive disruption distance, the peak should move to even lower values. We discuss this in the subsequent section.

The observed semi-major axis distribution is wider with a range  $\simeq 0.015 - 0.1$  AU. The overall shape of the observed distribution differs from that of the simulation, peaking towards larger values  $\simeq 0.04 - 0.05$  AU and with a more symmetrical shape around this peak.

We conclude that the semi-major axis distribution of Hot Jupiters formed in our fiducial simulation disagrees with the observations because it produces too many planets with  $a < 0.04$  AU relative to the number of planets with  $a > 0.04$  AU compared to the observed

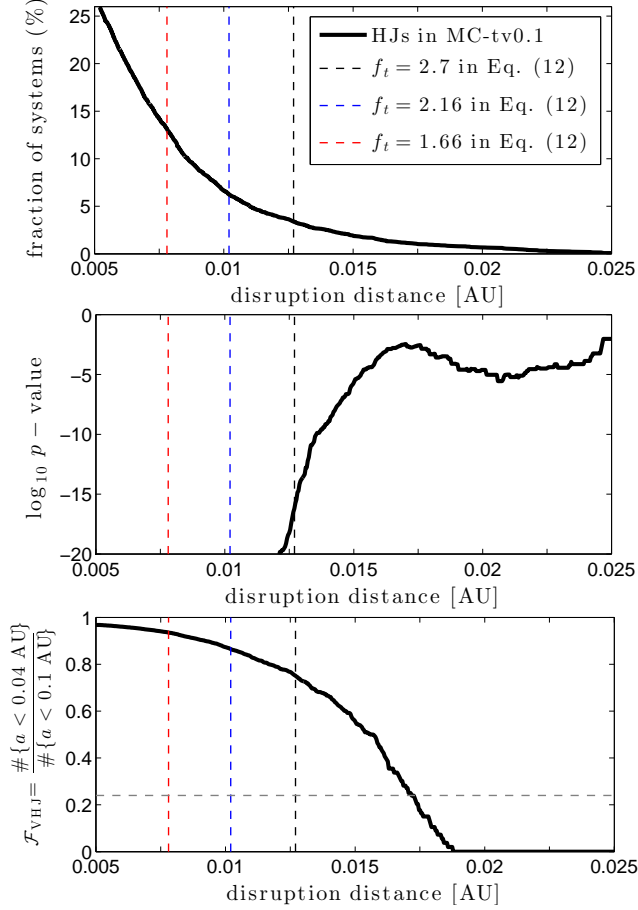


FIG. 5.— Hot Jupiters formed in MC-tv0.1 as a function of the disruption distance (or different values of  $R_t$  by changing  $f_t$  in Eq. [14]). *Upper panel:* fraction of systems forming Hot Jupiters. *Middle panel:*  $p$ -value from a K-S test between the observed semi-major distribution and that from the simulation. *Lower panel:* ratio between the number of Very Hot Jupiters ( $a < 0.04$  AU) and the number of Hot Jupiters ( $a < 0.1$  AU) ( $\mathcal{F}_{\text{VHJ}}$  in Eq. [16]), where the horizontal dashed line shows this ratio for the observed sample. The fraction of systems that would form a HJ if the disruption boundary is  $\simeq 0.005$  AU (star-planet collision) is  $\simeq 26\%$  (see MC-tv0.1-td in Table 1). The vertical black, blue, and red dashed lines indicate  $R_t$  from Equation (14) with  $f_t = 2.7$ ,  $f_t = 2.16$ , and  $f_t = 1.66$ , respectively.

sample.

In what follows we study how the different parameters in our simulation (Table 1) can affect the semi-major axis distribution. We ignore Spin-tv0.1 in this analysis because the semi-major axis distribution of the HJs in this simulation is essentially the same as that in our fiducial simulation.

### 5.1. Dependence on the disruption distance

Recall that we evolve the planets in the simulation MC-tv0.1 even after they crossed the disruption distance  $R_t$  with  $f_t = 2.7$  in Equation (14) and stopped the simulation only when the planet collides with star (i.e.,  $a(1-e) < R_\odot + R_J$ ).

The limiting scenario in which tidal disruption happens only when the planet collides with the star is given by MC-tv0.1-td where we set the tidal disruption distance to  $R_t = R_\odot + R_J$  (Eq. [14]). Collisions in MC-tv0.1-nt happen in  $\simeq 2\%$  of the systems (Table 1) when the perturber is strong enough: median  $a_{\text{out}}(1-e_{\text{out}})^{1/2} \simeq$

78 AU, consistent with the expectation that collisions happen when  $r_{\text{p,c}} < R_\odot + R_J \simeq 0.005$  AU (Eq. [8]).

We record the time whenever a new minimum pericenter is reached, which allows us to study the effect of the disruption distance on the production of Hot Jupiters.

In the upper panel of Figure 5, we show the fraction of HJs formed for a given disruption distance (i.e., different values of  $R_t$  or of  $f_t$  in Eq. [14]). The maximum fraction of HJs that can be formed is  $\simeq 26\%$ , by assuming that planets are only disrupted by collisions with the star. We observe that the fraction decreases dramatically as  $R_p$  increases. For  $f_t = 2.7$  in Equation (14), we have the fraction of 3.4% HJs reported in Table 1, while using  $f_t = 2.12$  this fraction increases to 6.3%. Moreover, for the disruption distance of 0.0078 AU (i.e.,  $f_t = 1.66$  in Eq. [14]) used in Naoz et al. (2012) we get a fraction of  $\simeq 13\%$  consistent with their similar simulation SMARan<sup>11</sup> which produces HJs in 13% of the systems.

In the middle panel of Figure 5, we show the  $p$ -value from a K-S test comparing the observed semi-major axis distribution and that from the simulation for a given disruption distance. Restricted to sample sizes of at least 10 HJs in the simulation, the maximum  $p$ -value is  $\simeq 0.0035$  for  $R_t = 0.017$  AU (i.e.,  $f_t = 3.6$  in Eq. [14]), which would result in a population of HJs with final semi-major axis  $> 0.034$  AU that represents a fraction of  $\simeq 1\%$  of all the systems.

In the lower panel of Figure 5, we show the ratio between the number of Very Hot Jupiters ( $a < 0.04$  AU) and the total number of Hot Jupiters ( $a < 0.1$  AU) ( $\mathcal{F}_{\text{VHJ}}$  in Eq. [16]). By decreasing disruption distance one allows for the formation of more HJs at smaller semi-major axis and, therefore,  $\mathcal{F}_{\text{VHJ}}$  increases. Recall that the observed sample has  $\mathcal{F}_{\text{VHJ}} \simeq 0.24$  (horizontal dashed line) and this ratio is reached in fiducial simulation by setting the disruption distance to  $\simeq 0.017$  AU (i.e., the same value for maximum  $p$ -value above). This ratio increases from  $\simeq 0.24$  at  $R_t \simeq 0.017$  AU to  $\simeq 0.75$  ( $\simeq 0.94$ ) when setting  $f_t = 2.7$  ( $f_t = 1.66$ ) in Equation (14).

As we decrease  $R_t$  from 0.017 AU to 0.005 AU, the  $p$ -value drops dramatically, while  $\mathcal{F}_{\text{VHJ}}$  departs from the observed value of  $\simeq 0.24$ . This is because the planets that reach small pericenters tend to migrate fast and their final semi-major axis is approximately twice the minimum pericenter distance reached during the simulation (see §3). This behavior implies that there is a pile-up of HJs at  $a \simeq 2R_t$ , like the one observed in Figure 4. Thus, by decreasing  $R_t$  this pile-up is shifted to lower values deviating from the observed peak at  $\simeq 0.04 - 0.05$  AU.

In summary, as we decrease the tidal disruption distance relative to our fiducial value the efficiency to produce HJs increases rapidly, while the semi-major axis distribution of the HJs formed starts rapidly deviating from that in the observed sample because too many planets are formed at very small semi-major axis. The observed semi-major axis distribution differs to that in the simulation for any disruption distance, while a coefficient of  $f_t \simeq 3.6$  in Equation (14) gives the least bad fit to the data.

<sup>11</sup> These authors used a different planetary viscous time of  $t_{\text{V},2} = 1.5$  yr and minimum semi-major axis of the perturber of  $a_{\text{out}} = 51$  AU.

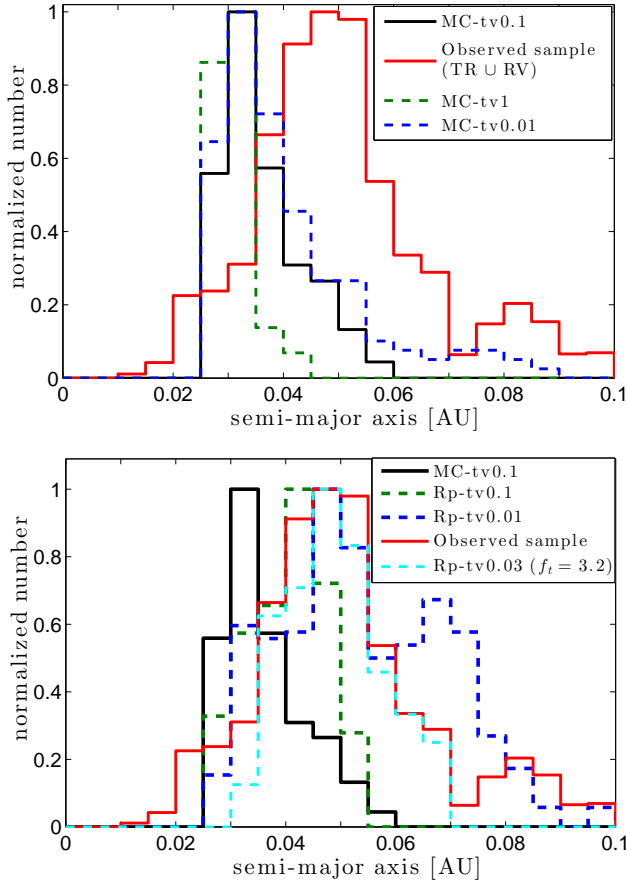


FIG. 6.— Semi-major axis distribution for the Hot Jupiters formed in the simulations MC-tv0.1 (black solid lines, upper and lower panels) and the observed sample (red solid lines, upper and lower panels). *Upper panel:* semi-major axis distribution in MC-tv1 (green dashed line) and MC-tv0.01 (blue dashed line). *Lower panel:* semi-major axis distribution in Rp-tv0.1 (green dashed line), Rp-tv0.01 (blue dashed line), and Rp-tv0.3 ( $f_t = 3.2$ ) (light blue dashed line). All histograms are normalized by the tallest bin. The bin width is 0.005 AU.

### 5.2. Dependence on tides

In the upper panel of Figure 6, we plot the semi-major axis distribution of Hot Jupiters for MC-tv1, MC-tv0.1, and MC-tv0.01 (see Table 1).

We observe that the fiducial simulation MC-tv1 is only able to form HJs with  $a < 0.045$  AU, which is consistent with our constraint in Equation (10) where by setting  $t_{V,2} = 1$  yr we find that the maximum semi-major axis that a planet can reach is  $\simeq 0.053$  AU. Since the semi-major axis distribution is narrower than in the fiducial simulation, the agreement with the observations is even worse. For instance,  $\mathcal{F}_{\text{VHJ}}$  in Equation (16) increases from  $\simeq 0.75$  in our fiducial simulation to  $\simeq 0.97$  (compared to 0.24 in the observed sample).

On the contrary, the simulation MC-tv0.01 gives rise to HJs up to  $\simeq 0.09$  AU, which is consistent with the prediction of Equation (10) that the maximum final semi-major axis is  $\simeq 0.098$  AU for  $t_{V,2} = 0.01$  yr. The semi-major axis distribution widens relative to the fiducial, which results in a slight decrease in  $\mathcal{F}_{\text{VHJ}}$  from  $\simeq 0.75$  in the fiducial simulation to  $\simeq 0.63$  (compared to 0.24 in the observed sample). However, the disagreement with the data is still present and is mostly due to the strong

pile-up of planets at  $\sim 0.03$  AU.

Similar to the previous subsection, we vary the disruption distance in MC-tv0.01 and determine which value gives the best agreement with data, based on a KS test and the ratio  $\mathcal{F}_{\text{VHJ}}$  in Equation (16). We find that the maximum  $p$ -value is  $\simeq 0.027$  for  $R_t = 0.016$  AU (i.e.,  $f_t = 3.4$  in Eq. [14]), which would result in a population of HJs with final semi-major axis  $> 0.032$  AU that represents a fraction of  $\simeq 3.6\%$  of all the systems with  $\mathcal{F}_{\text{VHJ}} = 0.24$  (similar to that in observed sample). This maximum  $p$ -value is higher than that from our fiducial simulation ( $\simeq 0.0035$ ) because for more efficient tidal dissipation HJs can be formed at larger semi-major axis, giving a better fit to the data.

In summary, we observe that the main effect of increasing the efficiency from tidal dissipation is to widen the semi-major axis distribution, which improves only slightly the agreement with the observations. However, the dominant feature of the semi-major axis distribution in our simulations is the strong pile-up of systems at the disruption boundary, which is off-set relative to the observed peak for our fiducial disruption distance. A model with a tidal disruption distance of 0.016 AU ( $f_t \simeq 3.4$  in Eq. [14]) and a planetary viscous time of 0.01 yr results in the least bad agreement with the observations.

### 5.3. Dependence on radius shrinkage

Gaseous giant planets are expected to form with large radii, which then shrink to the current observed values of  $\simeq 1R_J$  as the planet cools down.

In Rp-tv0.1 and in Rp-tv0.01 (Table 1) we prescribe the evolution of the planetary radius following Wu et al. (2007) as

$$R_p(t) = R_J [1 + \exp(-t/3 \cdot 10^7 \text{yr})], \quad (17)$$

which is an arbitrary functional form, but roughly describes the radius evolution from cooling models of Jupiter-like planets which predict shrinking timescales of  $\sim 10^7$  yr (e.g., Burrows et al. 1997).

In the lower panel of Figure 6, we show the semi-major axis distribution of the HJs formed in Rp-tv0.1 ( $t_{V,2} = 0.1$  yr) and Rp-tv0.01 ( $t_{V,2} = 0.01$  yr). We compare this distribution with that from our fiducial simulation MC-tv0.1 and the observed sample.

We observe that the semi-major axis distribution in Rp-tv0.1 peaks at  $a \sim 0.04$  AU and has a symmetrical shape in the range  $a \simeq 0.025 - 0.55$  AU: the mean (median) semi-major axis is 0.042 AU (0.043 AU). This is in sharp contrast with the fiducial simulation where we observe a strong pile-up of systems at  $a \simeq 0.025$  AU, which is set by the disruption distance (see §5.1). Since the disruption distance is proportional to the planetary radius (Eq. [14]), such distance in Rp-tv0.1 is initially larger by a factor of two compared to that from the fiducial simulation ( $t = 0$  in Eq. [17]). Therefore, if a planet migrates within  $10^7$  yr its semi-major axis is constrained to  $\gtrsim 0.043$  AU (set  $t < 10^7$  yr in Eqs. [11], [14], and [17]), which explains the deficit of planets at  $\simeq 0.025 - 0.03$  AU relative to the fiducial simulation. Note that an important fraction of planets are indeed able to migrate fast up to a final semi-major axis  $\gtrsim 0.043$  AU since tidal dissipation is greatly increased by the larger planetary radii: by setting  $R_2 = 2R_J$  in Equation (11) we get  $a_F > 0.043$  AU

for a perturber with  $a_{\text{out}}(1 - e_{\text{out}}^2)^{1/2} > 250$  AU, which corresponds to  $\sim 60\%$  of the systems.

The semi-major axis distribution of HJs in Rp-tv0.1 is able to reproduce the position of the peak in the observed sample: the median semi-major axis in Rp-tv0.1 is  $\simeq 0.043$  AU, while the observed HJs have a median of  $\simeq 0.045$  AU. Also the fraction of Very Hot Jupiters decreases from  $\mathcal{F}_{\text{VHJ}} \simeq 0.75$  to  $\mathcal{F}_{\text{VHJ}} \simeq 0.42$  (compared to  $\simeq 0.24$  in the observations). However, there are no planets at  $a > 0.06$  in Rp-tv0.1 because tides are not strong enough to allow planets to migrate to these separations, similar to what happens in the fiducial simulation (from Eq. [11] the migration timescale to form a HJ at  $\simeq 0.07$  AU is  $\sim 10$  Gyr whether or not shrinkage according to Eq. [17] is included).

In Rp-tv0.01 we have increased the efficiency of tides, so HJs at  $a > 0.06$  AU are able to form. From the lower panel of Figure 5 we observe that the semi-major axis distribution widens significantly compared to Rp-tv0.1: the mean (median) semi-major axis in Rp-tv0.01 is 0.062 AU (0.062 AU), while  $\mathcal{F}_{\text{VHJ}} \simeq 0.19$ . Thus, the semi-major axis distribution has shifted to values that are larger than the observed distribution and a KS test between the observed sample and Rp-tv0.01 yields  $p$ -value of  $\sim 3 \cdot 10^{-4}$ .

The fact that the mean and median of observed semi-major axis is bracketed by the results from Rp-tv0.1 and Rp-tv0.01, suggests that there should be a value of  $t_{V,2} = 0.01$ – $0.1$  and/or functional form of  $R_p(t)$  that fits the observations better. We have not carried a parameter survey, but we tried an extra simulation Rp-tv0.03 in which  $t_{V,2} = 0.03$  yr,  $R_p(t) = R_J (1 + 0.5 \cdot \exp(-t/3 \cdot 10^7 \text{yr}))$ , and  $f_t = 3.2$  in Equation (14) that fits the semi-major axis distribution much better ( $p$ -value is  $\sim 0.1$ ).

In summary, the planetary radius shrinkage reduces the production of HJs with small semi-major axes, while shifting the peak of the distribution to larger values. These effects result in a better fit to the observations compared to a model in which the planet’s radius remains constant in time.

#### 5.4. Dependence on the perturber

In §3 we argued that planets undergoing fast KL migration would reach a final semi-major axis  $a_F$  given by Equation (11). This expression for  $a_F$  is only approximate and ignores the planetary and stellar spins, which can change the angular momentum of the planetary orbit during migration.

In Figure 7, we show the final semi-major axis  $a_F$  from Equation (11) as a function of the final semi-major axis reached in MC-tv0.1-nt (planets are only destroyed by collisions). For each HJ formed in MC-tv0.1-nt we calculate  $a_F$  using the same input parameters that go into Equation (11) and use the corresponding semi-major axis and eccentricity of the perturber, so:  $a_F = 0.012 \text{ AU } (a_{\text{out}}(1 - e_{\text{out}}^2)^{1/2}/100 \text{ AU})^{3/6.5}$ .

We observe that the analytical expression gives a fair description of the results in MC-tv0.1-nt at small  $a$ : relative differences between  $a_F$  and final  $a$  are within  $\sim 30\%$  ( $\sim 50\%$ ) for  $a < 0.02$  AU ( $a < 0.03$  AU). This indicates that most of these planets have undergone fast KL migration and since  $\simeq 90\%$  of the HJs in MC-tv0.1-nt have  $a < 0.03$  AU, we conclude that fast (as opposed to slow) KL migration is the dominant migration regime.

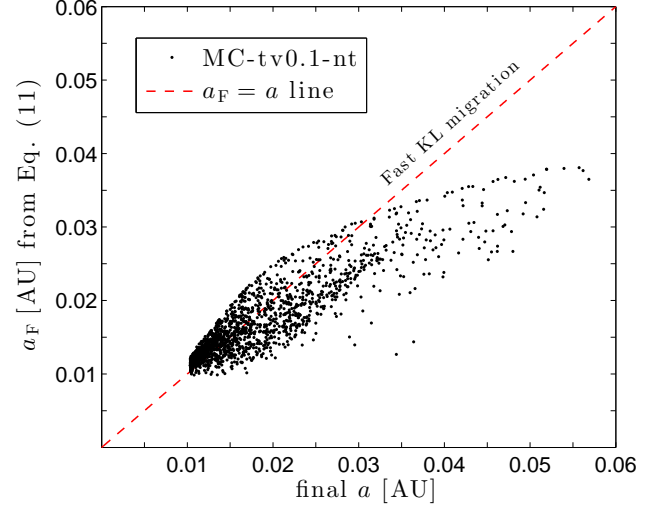


FIG. 7.— Final semi-major axis predicted from fast KL migration ( $a_F$  from Equation [11]) as a function of the final semi-major axis obtained for the Hot Jupiters in MC-tv0.1-nt (see Table 1). We calculate  $a_F$  using the parameters in MC-tv0.1-nt and the properties of the perturber (i.e.,  $a_{\text{out}}(1 - e_{\text{out}}^2)^{1/2}$ ) corresponding to each system. The red dashed line is the straight line  $a_F = a$  for visual comparison.

In contrast, the agreement with the analytical expression gets worse as we increase  $a$  (see deviations from the red dashed line). In particular, we observe that HJs at  $a \gtrsim 0.03$  AU have migrated to larger separations relative to what is predicted by  $a_F$ . This is because most of these planets have undergone slow KL migration and, therefore, reach larger semi-major axis by dissipating orbital energy through a sequence of many high-eccentricity cycles.

Since fast KL migration is the dominant migration channel, our results suggest that by having a weaker perturber (lower mass and angular momentum) we can shift the final semi-major distribution to larger values (see  $a_F$  from Eq. [11]). We test this hypothesis by running the simulations Mass-tv0.1 and Ecc-tv0.1 (Table 1).

In Mass-tv0.1 we decrease the mass of the perturber from  $m_3 = 1M_\odot$  in the fiducial simulation to  $m_3 = 0.1M_\odot$ , which implies an increase of  $\sim 40\%$  in  $a_F$  ( $\propto m_3^{-1/6.5}$ ) from Equation (11) relative to the fiducial simulation. The semi-major axis distribution (not shown) is almost identical to the fiducial simulation (see Figure 4) because even by shifting the semi-major axis of the planets at small separations to larger distances these still pile-up at the disruption distance. In particular, the fraction of VHJs decreases only slightly from  $\mathcal{F}_{\text{VHJ}} \simeq 0.75$  in the fiducial simulation to  $\mathcal{F}_{\text{VHJ}} \simeq 0.70$  in Mass-tv0.1. The maximum  $p$ -value is  $\simeq 0.001$  for  $R_t = 0.017$  AU (i.e.,  $f_t = 3.6$  in Eq. [14]), which is similar to the value found in the fiducial simulation of  $\simeq 0.003$ . However, the fraction of HJs formed using  $R_t = 0.017$  AU increases from  $\simeq 1\%$  in the fiducial simulation to  $\simeq 2\%$ . Similarly, from Table 1 we observe that the number of HJs formed ( $f_t = 2.7$  in Eq. [14]) also increases from  $\simeq 3.5\%$  in the fiducial simulation to  $\simeq 5\%$ . This difference is at the expense of having less tidal disruptions per HJ in systems with less massive perturbers: for weaker perturbers planets undergoing fast KL migration reach larger final semi-major axis (Eq. [11]) and can more easily avoid

disruption.

In Ecc-tv0.1 we change the eccentricity distribution of the binary from thermal with maximum eccentricity of 0.9 ( $U(e_{\text{out}}^2; 0, 0.81)$ ) in the fiducial simulation to a uniform distribution with maximum eccentricity of 0.95 ( $U(e_{\text{out}}; 0, 0.95)$ ). The semi-major axis distribution (not shown) is almost identical to that in the fiducial simulation (see Figure 4). The fraction of VHJs decreases only slightly from  $\mathcal{F}_{\text{VHJ}} \simeq 0.75$  in the fiducial simulation to  $\mathcal{F}_{\text{VHJ}} \simeq 0.67$  in Mass-tv0.1. The maximum  $p$ -value is  $\simeq 0.007$  for  $R_t = 0.018$  AU (i.e.,  $f_t = 3.8$  in Eq. [14],  $\simeq 1.2\%$  of HJs), which is slightly higher than the value found in the fiducial simulation of  $\simeq 0.003$ . Since a uniform distribution of binary eccentricities produces in average weaker perturbers compared to a thermal distribution, the number of disruptions per HJ decreases slightly relative to the fiducial simulation.

In summary, most HJs have undergone fast, instead of slow, KL migration and the approximate expression for the final semi-major axis (Eq. [11]) works well for HJs with  $a \lesssim 0.03$  AU. According to this expression, weaker perturbers (i.e., less massive, less eccentric, and/or more distant) produce HJs at larger semi-major axes, as we observe in the simulations, and are more likely to match the observations better. However, decreasing the mass by a factor of 10 and having a uniform eccentricity distribution of the perturber did not change the results significantly because the planets still pile-up at the disruption distance, a feature that dominates the semi-major axis distribution.

## 6. STELLAR OBLIQUITY DISTRIBUTION OF HOT JUPITERS

In Figure 8 we show the final distribution of the angle between the spin axis of the host star and the normal of the planetary orbit  $\psi$  (often called the stellar obliquity angle or misalignment angle) for the Hot Jupiters formed in MC-tv0.1 (solid black line in upper and lower panels), SMA500e0 (red dashed line in upper panel), MC-tv0.01 (blue dashed line in middle panel), MC-tv0.1-nt (red dashed line in middle panel), and Spin-tv0.1 (red dashed line in lower panel).

We observe that the distribution of the stellar obliquity in our fiducial simulation MC-tv0.1 ranges from  $\psi \simeq 10^\circ - 170^\circ$  and is roughly flat for  $\psi \simeq 10^\circ - 140^\circ$ , with a mean (median) of  $\simeq 78^\circ$  ( $\simeq 74^\circ$ ). The fraction of retrograde systems ( $\psi > 90^\circ$ ) in MC-tv0.1 is  $\simeq 38\%$ , which is consistent within Poisson the errors with the fraction of  $\simeq 44\%$  found by Naoz et al. (2012) in similar simulations.

### 6.1. Quadrupole- vs octupole-level gravitational interactions

In the panel a of Figure 8 we compare the results of our fiducial simulation MC-tv0.1 with SMA500e0. The latter simulation is identical to that from Fabrycky & Tremaine (2007) (see figure 10 therein), which has a perturber with fixed semi-major axis  $a_{\text{out}} = 500$  AU and eccentricity  $e_{\text{out}} = 0$  so the octupole-level contribution to the gravitational interaction vanishes. Thus, comparing SMA500e0 to our fiducial simulation illustrates the role of these higher-order contributions to the potential in shaping the obliquity distribution.

We observe that the distribution of the obliquity in

SMA500e0 ranges from  $\psi \simeq 0^\circ - 140^\circ$  and is skewed towards low values relative to MC-tv0.1: the mean (median) in SMA500e0 is  $\simeq 49^\circ$  ( $\simeq 43^\circ$ ), compared to  $\simeq 78^\circ$  ( $\simeq 74^\circ$ ) in MC-tv0.1. SMA500e0 has a significant deficit of systems relative to MC-tv0.1 at all obliquities  $\psi \gtrsim 60^\circ$ .

The fraction of retrograde systems ( $\psi > 90^\circ$ ) in MC-tv0.1 is  $\simeq 38\%$ , while it decreases to  $\simeq 15\%$  in SMA500e0.

We conclude that the octupole-level gravitational interactions can have a significant effect on broadening the obliquity distribution. This result is consistent with Naoz et al. (2012), who argue that by adding the octupole order term in the potential the planetary orbit can reach more extreme mutual inclinations, which produce a flatter distribution of  $\psi$ .

### 6.2. Effect of tidal dissipation and disruption distance

In the panel b of Figure 8 we compare the obliquity distribution of our fiducial simulation MC-tv0.1 with MC-tv0.01 and MC-tv0.1-nt to study the effect of the strength of tidal dissipation and the disruption distance, respectively.

The obliquity distribution has a similar overall shape in all three simulations and is more or less flat for  $\psi \simeq 20^\circ - 130^\circ$ . However, both MC-tv0.01 and MC-tv0.1-nt show a marginally significant excess (deficit) of systems with  $\psi = 0 - 10^\circ$  and  $\psi = 110^\circ - 120^\circ$  ( $\psi = 130^\circ - 140^\circ$ ) relative to the fiducial simulation. The mean (median) in MC-tv0.01 and MC-tv0.1-nt is  $\simeq 72^\circ$  ( $\simeq 67^\circ$ ) and  $\simeq 75^\circ$  ( $\simeq 74^\circ$ ), compared to  $\simeq 78^\circ$  ( $\simeq 74^\circ$ ) in MC-tv0.1. The fraction of retrograde systems ( $\psi > 90^\circ$ ) in MC-tv0.01 is  $\simeq 35\%$  and  $\simeq 38\%$  in MC-tv0.1-nt, similar to the fiducial simulation with  $\simeq 38\%$ .

A KS test comparing the obliquity distribution obtained from the fiducial simulation MC-tv0.1 and MC-tv0.01 (MC-tv0.1-nt) results in a  $p$ -value of  $\simeq 0.1$  ( $\simeq 0.13$ ). Thus, at the 90% confidence level the obliquity distributions in MC-tv0.1, MC-tv0.01, and MC-tv0.1-nt are all consistent with one another.

In conclusion, changing the amount of tidal dissipation and ignoring planetary tidal disruptions have no significant effect on the distribution of stellar obliquities.

### 6.3. Effect of host star's spin period

In the panel c of Figure 8 we compare the obliquity distribution of our fiducial simulation MC-tv0.1 with Spin-tv0.1 to study the effect of decreasing the initial host star's spin period from our fiducial value of 10 days to 3 days. We note that host stars with giant planets are observed to have rotation periods of  $\sim 2 - 20$  days (e.g., Walkowicz & Basri 2013).

We observe that the obliquity distribution of HJs in Spin-tv0.1 differs significantly relative to our fiducial simulation and becomes bimodal peaking at  $\psi \sim 20^\circ - 40^\circ$  and  $\psi \sim 110^\circ - 140^\circ$ . By decreasing the period of the host star the distribution shows a significant deficit of HJs with  $\psi \sim 40^\circ - 110^\circ$  relative to MC-tv0.1.

This bimodality in the obliquity distribution has been recently discovered by Storch et al. (2014) and it has been attributed to the chaotic behavior of the host star's spin axis during KL migration. As Storch et al. (2014) describe, this behavior happens when the precession frequency due to planetary orbit and the rotation-induced

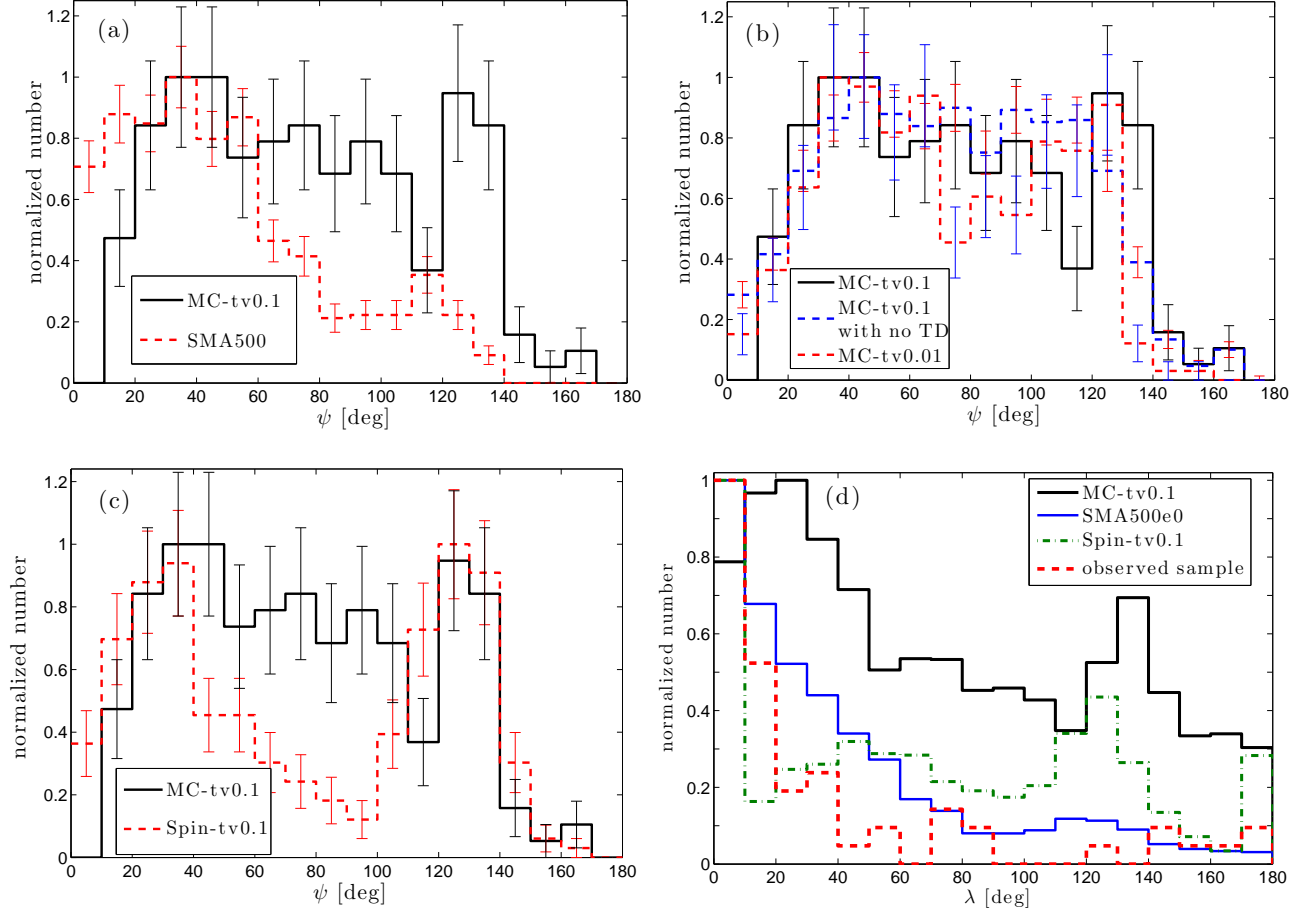


FIG. 8.— Final distribution of the angle between the spin of the host star and the normal of the planetary orbit  $\psi$  (often called stellar obliquity or misalignment angle) and its sky-projected value  $\lambda$  for the HJs formed in the simulations and observations as labeled. *Panel a*: the results for MC-tv0.1 (solid black line) and SMA500e0 (red dashed line). *Panel b*: the results for MC-tv0.1 (solid black line), MC-tv0.01 (blue dashed line), and MC-tv0.1-nt (red dashed line). *Panel c*: the results for MC-tv0.1 (solid black line) and Spin-tv0.1 (red dashed line). *Panel d*: the results for MC-tv0.1 (solid black line), SMA500e0 (solid blue line), Spin-tv0.1 (green dot-dashed line), and the observed sample of HJs (red dashed line). The error bars indicate the  $1\sigma$  confidence limits from the Poisson counting errors for each bin. The bin width is  $10^\circ$ .

stellar quadrupole (proportional to the host star’s spin frequency) roughly matches the precession frequency of the planet’s orbital angular momentum vector due to the binary companion. In our fiducial simulation, the former frequency is generally less than the latter during the formation of the HJs and, therefore, the spin axis of the host star remains roughly unaffected by the torque due to the planet. On the contrary, by increasing host star’s spin frequency in Spin-tv0.1 these precession frequencies can be comparable in most cases during the formation of the HJ leading to a different host star’s spin axis behavior and modifying the obliquity distribution.

We conclude that by decreasing the host star’s spin period the distribution of obliquities becomes bimodal in our simulations. This result is consistent with Storch et al. (2014) and, based on their work, a similar behavior is expected when increasing the mass of the planets in our simulations.

As of January 2013, the observed sample of Hot Jupiters<sup>12</sup> (planets with  $M \sin(i) > 0.1M_J$  and  $a < 0.1$  AU) contains 56 planets with projected stellar obliquity measurements  $\lambda$ .

In panel d Figure 8 we show the projected obliquity distribution from the observed sample and that from our fiducial simulation MC-tv0.1 and SMA500e0. The projection of  $\psi$  (see Figure 8) is calculated by taking  $10^5$  random orbital configurations relative to a fixed observer for each simulated system (see e.g., Fabrycky & Winn 2009). We observe that the fiducial simulation produces too many systems with large projected obliquities relative to the observed sample. For instance, the observations show that only  $\simeq 40\%$  ( $\simeq 35\%$ ) of planets have  $\lambda > 20^\circ$  ( $\lambda > 30^\circ$ ), while  $\simeq 83\%$  ( $\sim 73\%$ ) of the HJs in MC-tv0.1 are in the same range of projected obliquities. If we assume that all the misaligned ( $\lambda > 20^\circ$ ) HJs are due to KL migration, one gets a crude upper limit to the fraction of systems that can be explained by the theory as: 40% from the misaligned sample plus a fraction of  $0.4/0.83$  of the  $\simeq 17\%$  of aligned planets in the theoretic

#### 6.4. Comparison with observations

<sup>12</sup> Taken from The Exoplanet Orbit Database (Wright et al. 2011)

cal distribution. This results in an upper limit of  $\simeq 48\%$  and a similar upper limit of  $\simeq 47\%$  results by considering the planets with  $\lambda > 30^\circ$  as the misaligned sample.

Our crude upper limit is consistent with Naoz et al. (2012) who found that KL migration can account for at most  $\sim 60\%$  (figure 4 therein) of the obliquity distribution, while it most likely accounts for  $\sim 30\%$  of the systems. These authors follow Morton & Johnson 2011 by taking into account the errors in the observed projected obliquities and they represent the theoretical obliquity distribution as the sum of three migration mechanisms: KL migration, planet-planet scattering, and disk migration.

In contrast, the simulation SMA500e0 which considers a non-eccentric stellar binary (i.e., no octupole-level gravitational interactions) produces more systems with small obliquities relative to the fiducial simulation. Therefore, the obliquity distribution of SMA500e0 compares more favorably with the observations than our fiducial simulation. A KS test comparing the obliquity distribution of SMA500e0 and the observed sample results in a  $p$ -value of  $\simeq 0.008$ .

Similarly, in our simulation with shorter initial host star's spin periods Spin-tv0.1 we get a better agreement with the observations compared with our fiducial simulation because the distribution of  $\lambda$  is skewed towards lower values which peaks at  $\lambda < 10^\circ$ . However, the HJs in Spin-tv0.1 tend to still be more misaligned than in the observations:  $\simeq 40\%$  ( $\simeq 35\%$ ) of planets have  $\lambda > 20^\circ$  ( $\lambda > 30^\circ$ ) in the observed sample, while  $\simeq 70\%$  ( $\simeq 63\%$ ) of the HJs in Spin-tv0.1 are in the same range of projected obliquities.

In summary, KL migration is unable to reproduce the obliquity distribution of HJs and by assuming that all the observed misaligned planets are due to KL migration, this mechanism can produce at most  $\sim 50\%$  of the planets. Simulations with only quadrupole-level gravitational interactions and shorter initial host star's spin periods show a better agreement with the data.

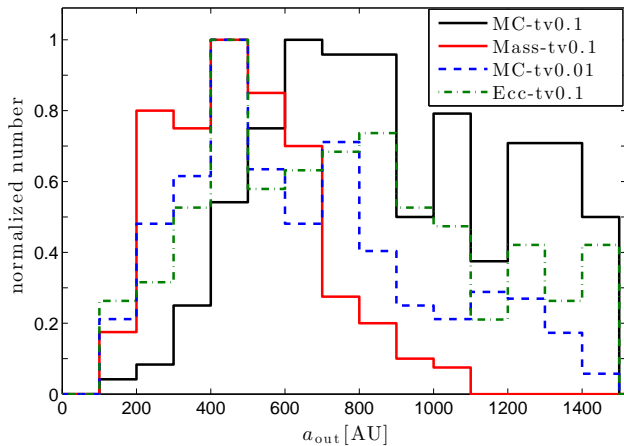


FIG. 9.— Distribution of the semi-major axis of the stellar binary for the systems that formed a Hot Jupiter in the simulations MC-tv0.1 (solid black line), Mass-tv0.1 (solid red line), MC-tv0.01 (blue dashed line), and Ecc-tv0.1 (green dotted-dashed line). See Table 1 for the description of each simulation. The bin size is 100 [AU].

## 7. HOT JUPITER SYSTEMS: FORMATION RATE AND BINARY COMPANIONS

### 7.1. Efficiency constraint from the semi-major axis distribution

As discussed in §5, the semi-major axis distribution of HJs formed by KL migration does not match the observed distribution unless we change the disruption distance or start the simulation with an inflated planet. In this subsection we use this mismatch to place constraints on the maximum contribution from KL migration to the observed population of HJs.

We build an approximate measure of the maximum fraction of systems  $\mathcal{F}_\lambda$  that the theoretical distribution  $Y_t$  can explain from the observed distribution  $Y_{\text{obs}}$  as

$$\mathcal{F}_\lambda = 1 - \min_{\lambda \in [0,1]} \sum_{i=1}^N |Y_{\text{obs}}^i - \lambda Y_t^i|, \quad (18)$$

where  $Y_{\text{obs}}^i$  and  $Y_t^i$  are the fraction of systems with  $a \in 0.1 \text{ AU}[(i-1)/N, i/N]$  with  $i = 1, \dots, N$  in the observed sample and the theoretical distribution. We calculate  $\mathcal{F}_\lambda$  by letting  $Y_{\text{obs}}^i$  take values within its  $1 - \sigma$  Poisson error bar for each bin  $i$ , but constrained to be normalized to one:  $\sum_{i=1}^N Y_{\text{obs}}^i = \sum_{i=1}^N Y_t^i = 1$ .

In Table 2, we show the values of  $\mathcal{F}_\lambda$  for a discretization of the semi-major axis in  $N = 10$  bins and using both the RV and transit planets (TR and TR2). In TR we correct the observed distribution by geometric bias ( $\propto a^{-1}$ ) only (as in the rest of the paper), while in TR2 we correct the observed distribution with a steeper function of the semi-major axis  $\propto a^{-5/2}$ , which takes into account both the transit probability and the detection probability for a given S/N (Gaudi et al. 2005). Our results for  $\mathcal{F}_\lambda$  change only slightly (by  $\sim 10\%$ ) for  $N = 5$  and  $N = 20$  bins.

The constraint from the RV sample is weaker (larger  $\mathcal{F}_\lambda$ ) than that from TR (and TR2) because the former has a smaller sample (37 planets) than the latter (159 planets). Moreover, TR2 is more constraining than TR because the former produces a distribution that favors planets with larger semi-major axes.

From Table 1, our fiducial simulation MC-tv0.1 can produce up to 44% of the HJs based on the RV sample and up to 37% (19%) based on the TR (TR2) sample. Such fractions decrease to  $< 6\%$  in MC-tv0.1-nt (i.e., ignoring tidal disruption). Thus, even though the number of HJs formed in MC-tv0.1-nt is higher than MC-tv0.1 by a factor of  $\simeq 8$  (Table 1), the production can be strongly constrained by the semi-major axis distribution.

Based on the TR sample we observe from Table 1 that the KL migration can explain up to  $\sim 40\%$  of the HJs if we ignore the simulations where the planetary radius shrinks (Rp-tv0.1, Rp-tv0.01, and Rp-tv0.03). This fraction goes down to  $\sim 20\%$  if we consider a steeper semi-major axis dependence for the selection biases.

We conclude that the semi-major axis distribution of HJs in the observed population places an upper limit of  $\sim 20 - 40\%$  to the overall production of HJs from KL migration due to binary companions. Such contribution can increase up to  $\sim 70\%$  if we start the simulations with an inflated planet.

### 7.2. Formation rate

Following Wu et al. (2007) we estimate the fraction of stars with Hot Jupiters ( $a < 0.1 \text{ AU}$ ) that have migrated

TABLE 2

HOT JUPITER SYSTEMS: MAXIMUM CONTRIBUTION TO THE OBSERVED SEMI-MAJOR AXIS DISTRIBUTION FROM  $\mathcal{F}_\lambda$  IN EQ. (18), PRODUCTION RATE, AND SEMI-MAJOR AXIS OF STELLAR BINARY

| Name        | $\mathcal{F}_\lambda$ in Eq. (18) | HJ production rate:          | $a_{\text{out}}$ [AU] |
|-------------|-----------------------------------|------------------------------|-----------------------|
|             | RV - TR - TR2 <sup>a</sup> (%)    | $f_{<0.1}$ from Eq. [19] (%) | mean - median         |
| MC-tv0.1    | 44 - 37 - 19                      | 0.092                        | 890 - 845             |
| MC-tv0.1-nt | 6 - 2 - 0.2                       | 0.73                         | 373 - 270             |
| MC-tv1      | 12 - 31 - 11                      | 0.042                        | 832 - 801             |
| MC-tv0.01   | 58 - 43 - 23                      | 0.21                         | 656 - 598             |
| Ecc-tv0.1   | 49 - 40 - 21                      | 0.089                        | 757 - 725             |
| Mass-tv0.1  | 48 - 35 - 19                      | 0.14                         | 490 - 470             |
| Spin-tv0.1  | 43 - 36 - 19                      | 0.092                        | 830 - 811             |
| Rp-tv0.1    | 64 - 61 - 41                      | 0.067                        | 701 - 678             |
| Rp-tv0.01   | 81 - 67 - 61                      | 0.17                         | 608 - 537             |
| Rp-tv0.03   | 82 - 83 - 73                      | 0.064                        | 834 - 793             |

<sup>(a)</sup>  $\mathcal{F}_\lambda$  in Eq. (18) is calculated using  $N = 10$  bins for different observed samples: RV (radial velocity planets), TR (transit planets corrected by geometric bias), and TR2 (transit planets corrected by assuming a detection probability  $\propto a^{-5/2}$ ).

by the KL mechanism as:

$$f_{<0.1} = f_b \cdot f_p \cdot f_{\text{KL}}, \quad (19)$$

where  $f_b$  is the fraction of stars in binaries,  $f_p$  is the fraction of Solar-type stars hosting a gas giant planet at a few AU, and  $f_{\text{KL}}$  is the fraction of Hot Jupiters formed by the KL mechanism in our simulations.

The fraction of solar-type stars in binary systems is  $\sim 65\%$  (Duquennoy & Mayor 1991; Raghavan et al. 2010), while the fraction of binary systems with  $a_{\text{out}} > 100$  AU estimated from the observed semi-major axis distribution is  $\sim 30\%$  (Raghavan et al. 2010; Eggenberger et al. 2011). Note that the efficiency from KL migration to form HJs in tighter binaries ( $a_{\text{out}} < 100$  AU) is negligible since HJs are typically formed in binaries with  $a_{\text{out}} > 200 - 400$  AU (see Figure 9 and the recent simulations by Martí & Beaugé 2014 for tighter binaries). Thus, we approximate the fraction of stars in binaries by restricting ourselves to wide binaries only, which results in  $f_b \sim 65\% \times 30\% \sim 20\%$ . Note also that the fraction of stars hosting planets in single stars is similar to that in wide binary stars (Raghavan et al. 2010).

The fraction of solar-type stars hosting a planet more massive than  $\simeq 0.15M_J$  on a orbit with a period shorter than 10 years is  $\simeq 14\%$  (Mayor et al. 2011), and most of these are beyond  $\sim 1$  AU. This fraction is consistent with the lower limit of 7% previously found by Marcy et al. (2005). Thus, the fraction of solar-type stars hosting a gas giant planet at a few AU is  $f_p \simeq 14\%$ . This number might be regarded as an upper limit since a fraction of these systems have multiple planets in which case the KL mechanism might not operate (e.g., Innanen et al. 1997; Fabrycky & Tremaine 2007).

The fraction of Hot Jupiters  $f_{\text{KL}}$  formed by the KL mechanism in our simulations is given in Table 1 and spans the range  $\simeq 1.4 - 7.4\%$ . This range is consistent with the previous estimates by Wu et al. (2007) who find  $f_{\text{KL}} \simeq 2.5\%$  using similar Monte Carlo simulations (although with a different prescription of tides<sup>13</sup> and ignoring the effect from octupole-level gravitational interactions).

<sup>13</sup> The authors assume that during migration  $Q$  is constant as opposed to a constant viscous time (or time-lag) that we assume in our simulations.

As discussed in §5.1, the fraction of HJs formed in our simulations increases rapidly for smaller values of the tidal disruption distance (see upper panel of Figure 5) and by considering a distance of 0.0078 AU (i.e.,  $f_t = 1.66$  in Eq. [14]) as in Naoz et al. (2012) we get a fraction of  $f_{\text{KL}} \simeq 13\%$  in our fiducial simulation, consistent with the results from these authors. However, as we decrease the tidal disruption distance the semi-major axis distribution from our model deviates more and more from the observed distribution (see middle and lower panel of Figure 5).

In Table 2, we show the estimated fraction of stars with Hot Jupiters produced by KL migration  $f_{<0.1}$  in Equation (19) by taking  $f_b = 0.2$ ,  $f_p = 0.14$ , and  $f_{\text{KL}}$  from Table 1 (i.e., with  $f_t = 2.7$  in Eq. [14]). We observe that such fraction ranges in  $f_{<0.1} = 0.042 - 0.21\%$ .

In contrast, the estimated overall occurrence rate of Hot Jupiters in FGK dwarfs is  $\simeq 0.9 - 1.5\%$  from RV surveys (Marcy et al. 2005; Mayor et al. 2011; Wright et al. 2012) and  $\simeq 0.3 - 0.5\%$  from TR surveys (Gould et al. 2006; Howard et al. 2012). The difference in the estimated rates from RV and TR surveys might be due to a difference in metallicity in both samples (Wright et al. 2012; Dawson & Murray-Clay 2013).

Based on the rates of HJs produced by KL migration and the observed rates in RV (TR) surveys, we infer that the overall contribution from KL migration to the Hot Jupiter population is  $\sim 3 - 23\%$  ( $\sim 8 - 70\%$ ). If tidal disruptions are ignored in our simulations (MC-tv0.1-nt), KL migration can contribute up to  $\sim 80\%$  ( $\sim 100\%$ ) based on the RV (TR) surveys, but such production rate is limited to  $< 6\%$  based on the semi-major axis distribution (see §7.1). Note that the overall fraction  $f_p$  of stars with giant planets is estimated from RV surveys and, therefore, it might more appropriate to compare our model with the HJ rate observed in the RV surveys rather than in the TR surveys.

In summary, based on the RV surveys only, KL migration due to stellar companions forms  $\sim 3 - 23\%$  of the Hot Jupiters. Such rate can increase up to  $\sim 80\%$  by decreasing the disruption distance, but is strongly limited by the observed semi-major axis distribution.

### 7.3. Semi-major axis of the stellar binaries

In Figure 9 we show the distribution of the semi-major axis of the stellar binary  $a_{\text{out}}$  for systems that formed a Hot Jupiter in MC-tv0.1 (solid black line), Mass-tv0.1 (solid red line), MC-tv0.01 (blue dashed line), and Ecc-tv0.1 (green dotted-dashed line). In Table 2 we show the mean and median  $a_{\text{out}}$  for these systems.

As discussed in §4.3 and shown in Figure 9, the fiducial simulation MC-tv0.1 forms HJs in systems with wide binaries (typically  $a_{\text{out}} = 500 - 1500$  AU), which is consistent with the simulations by Naoz et al. (2012).

From Figure 9 we observe that as we decrease the mass of the perturber from  $1M_{\odot}$  in the fiducial simulation to  $0.1M_{\odot}$  in Mass-tv0.1 the distribution of the semi-major axis of the binary in Hot Jupiter systems narrows and shifts to lower values: the median  $a_{\text{out}}$  decreases from 845 AU in the fiducial simulation to 470 AU in Mass-tv0.1 (Table 2). In contrast, most HJs in Mass-tv0.1 are found in binaries with  $a_{\text{out}} = 200 - 700$  AU, which is roughly the range found in our fiducial simulation of  $a_{\text{out}} = 500 - 1500$  AU divided by  $\sim 2$ . This is expected because the mass of the perturber only affects the KL timescale as  $\tau_{\text{KL}} \propto a_{\text{out}}^3/m_3$  (Eq. [1]), so at fixed KL timescale  $a_{\text{out}} \propto m_3^{1/3}$ , which corresponds to a factor of  $\sim 2$  decrease in  $a_{\text{out}}$  when the mass of the binary companion is reduced by 10.

By changing the binary eccentricity distribution from thermal in the fiducial simulation to uniform in Ecc-tv0.1 we observe that the distribution of the semi-major axis of the binary narrows, but only slightly (Figure 9).

From Figure 9 we also observe that by increasing the amount of tidal dissipation from  $t_{V,2} = 0.1$  yr in the fiducial simulation to  $t_{V,2} = 0.01$  yr in MC-tv0.1 the distribution of  $a_{\text{out}}$  shifts to lower values: the median  $a_{\text{out}}$  decreases from 845 AU in the fiducial simulation to 598 AU in MC-tv0.01 (Table 2). Also, the formation of HJs in MC-tv0.01 is more efficient by  $\simeq 2.2$  (Table 1) and by  $\sim 10$  in  $a_{\text{out}} = 100 - 400$  than in the fiducial simulation.

We conclude that stellar companions in systems with Hot Jupiters are expected to be preferentially found at wide separations:  $a_{\text{out}} \simeq 400 - 1500 (m_3/1M_{\odot})^{1/3}$  AU. The formation of HJs in binaries with relatively small separations ( $a_{\text{out}} \lesssim 400$  AU) is more likely for planets with more efficient tidal dissipation.

## 8. FORMATION OF INTERMEDIATE PERIOD PLANETS

From Table 1 we observe that the fraction of migrating planets ( $0.1 \text{ AU} < a < 4.5 \text{ AU}$ ) is less than  $\sim 1\%$  in all simulations (see also panel (a) of Figure 3). Thus, KL migration is very inefficient at producing planets with intermediate periods ( $\sim 10 \text{ d} - 3 \text{ yr}$ , or  $a \sim 0.1 - 2 \text{ AU}$ ).

This lack of intermediate period planets is due to two different effects:

- many planets undergo fast KL migration (according to the definition in §3) in which case the time spent at intermediate periods is negligible compared to the planet's lifetime;
- if the planets undergo slow KL migration (see HJs close to the dashed line in panel (c) of Figure 3), they spend most their lifetimes either undergoing KL oscillations at long periods ( $> 3 \text{ yr}$ ) or as HJs

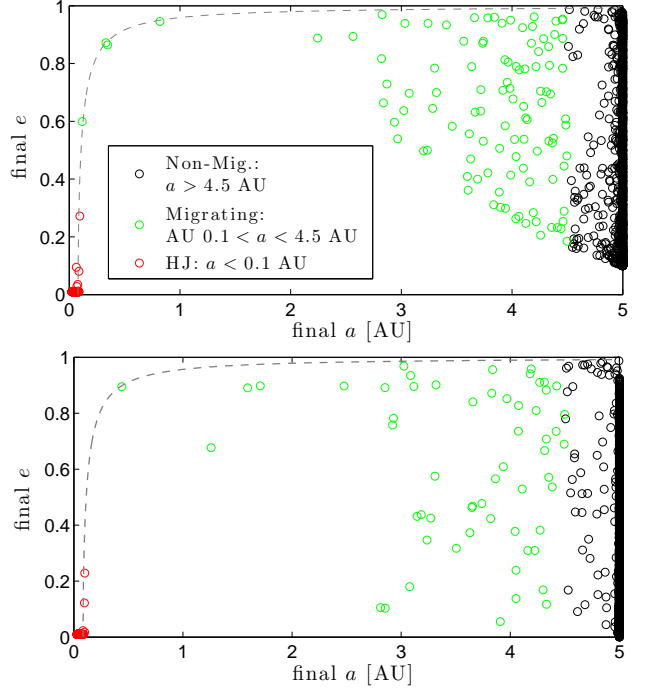


FIG. 10.— Final semi-major axis and eccentricity of the planetary orbit for simulations SMA500e0 (upper panel) and Rp-tv0.01 (lower panel), similar to the panel (a) in Figure (3). The dashed lines indicated the constant angular momentum tracks:  $a(1-e^2) = 0.08 \text{ AU}$ .

(see discussion in §2 and red line in the lower panel of Figure 1).

In Figure 10 we show the final semi-major axis and eccentricity for the planets in the two simulations that have the highest fraction of migrating planets (see Table 1): SMA500e0 (upper panel) and Rp-tv0.01 (lower panel).

We observe that both SMA500e0 and Rp-tv0.01 have 4 planets with  $a = 0.1 - 2 \text{ AU}$ . The former simulation has all four planets following a constant angular momentum track  $a(1-e^2) \simeq 0.08 \text{ AU}$  because the perturber has  $a_{\text{out}} = 500 \text{ AU}$  and the oscillations are quenched by GR at  $a \sim 1.5 \text{ AU}$  (see Figure 1). The latter simulation has only one planet following the track  $a(1-e^2) \simeq 0.08 \text{ AU}$ , while the other three are found off the migration track undergoing KL oscillations. These three planets have a perturber with  $a_{\text{out}} \sim 200 \text{ AU}$  so KL oscillations are quenched at  $a \lesssim 1 \text{ AU}$  and given that the planetary radius shrinks, the migration occurs much faster during the first  $\sim 10^7 \text{ yr}$  and then slows down making it more likely to form intermediate period planets.

### 8.1. Steady flow of migrating planets

Following Socrates et al. (2012a), the expected number density of planets with a given eccentricity in a constant angular momentum track  $J$  can be estimated as (Eqs. 7 and 10 therein)

$$\frac{dN_J(e)}{de} \simeq C_J \frac{1}{e(1-e^2)^{3/2}(2.33 + 6.12e^3)}, \quad (20)$$

where  $C_J$  is a constant proportional to the current of migrating planets with angular momentum in  $(J, J+dJ)$ .

By integrating Equation (20) one can estimate the ratio between the number of moderately eccentric ( $e =$

0.2 – 0.6) planets and the number of highly eccentric planets, which we define as  $e = 0.85 - 0.99$  (at the migration track  $a(1 - e^2) \simeq 0.08$  AU, the upper limit of 0.99 implies  $a < 4$  AU). By considering the planets that lie in the angular momentum bin  $a(1 - e^2) = 0.06 - 0.1$  AU, this ratio is 1.5 and 1 in SMA500e0 and Rp-tv0.01, which is consistent with the  $\simeq 1.4$  that results from integrating Equation (20) (although there are too few planets in the simulations to make a more thorough comparison with Socrates et al. 2012a).

In the RV sample there are 37 giant planets ( $M \sin i > 0.1 M_J$ ) with  $a < 0.1$  AU, 4 giant planets with moderate eccentricities in  $a(1 - e^2) = 0.06 - 0.1$  AU and 2 giant planets in highly eccentric orbits: HD 80606b (Naef et al. 2001) and HD 20782b (O’Toole et al. 2009), both of which are in binary stellar systems. By limiting to orbital periods  $< 2$  yr and defining a highly eccentric planet at  $e > 0.9$  Socrates et al. (2012a) argue that given the four moderately eccentric planets one would expect 2 – 3 planets with high eccentricities, which is consistent with the observations. Consistently, the simulation SMA500e0 has 2 moderately eccentric planets and one highly eccentric planet. Again, the simulations and the RV sample have too few planets as to make a more thorough comparison and the RV surveys are biased against detecting highly eccentric planets (e.g., Cumming 2004). In any case, the simulation SMA500e0 forms  $\sim 300$  HJs per moderately eccentric planet which is very large compared with the  $\sim 10$  HJs in the RV sample.

In order to avoid selection biases against finding highly eccentric planets, Socrates et al. (2012a) proposed to study the flow of migrating planets using the *Kepler* sample. By constraining the eccentricity from transit light curves in *Kepler* (see Dawson & Johnson 2012), Dawson et al. (2012) report a null detection of highly eccentric planets ( $e > 0.9$ ) in sample of 41 candidates with  $a \simeq 0.2 - 1.6$  AU (orbital periods of  $\simeq 36$  d – 2 yr). In order to compare this observation with the expected number of highly eccentric planets, these authors consider a sample of 31 (19) Hot Jupiters with  $a \simeq 0.04 - 0.06$  AU ( $a \simeq 0.06 - 0.1$  AU) and use the RV sample to estimate a number of moderately eccentric planets. Their estimates indicate that KL migration can only produce  $0.15^{+0.29}_{-0.11}$  of the HJs in *Kepler*.

Our simulations show that the lack of highly eccentric planets observed by Dawson et al. (2012) is expected from KL migration. For instance, the fiducial simulation MC-tv0.1 is able to form 51 HJs with  $a \simeq 0.04 - 0.06$  AU (all with  $e \simeq 0$ ) and only one highly eccentric planet with  $a = 0.2 - 1.6$  AU (see panel a of Figure 3). Similarly, Rp-tv0.01 forms 151 (122) HJs with  $a = 0.04 - 0.06$  AU ( $a = 0.06 - 0.01$  AU) and only one moderately eccentric HJ and one highly eccentric planet (see lower panel of Figure 10). Note, however, that the total number of HJs relative to the number of moderately eccentric HJs is much larger in the simulations than in the RV sample. Since the eccentricities of the four moderately eccentric planets in the observed sample are  $e \sim 0.3 - 0.5$  overestimates due to bias in RV measurements are unlikely to account for the difference between our simulation and the data (Zakamska et al. 2011).

In summary, despite the low number of planets in a migration track at constant angular momentum found

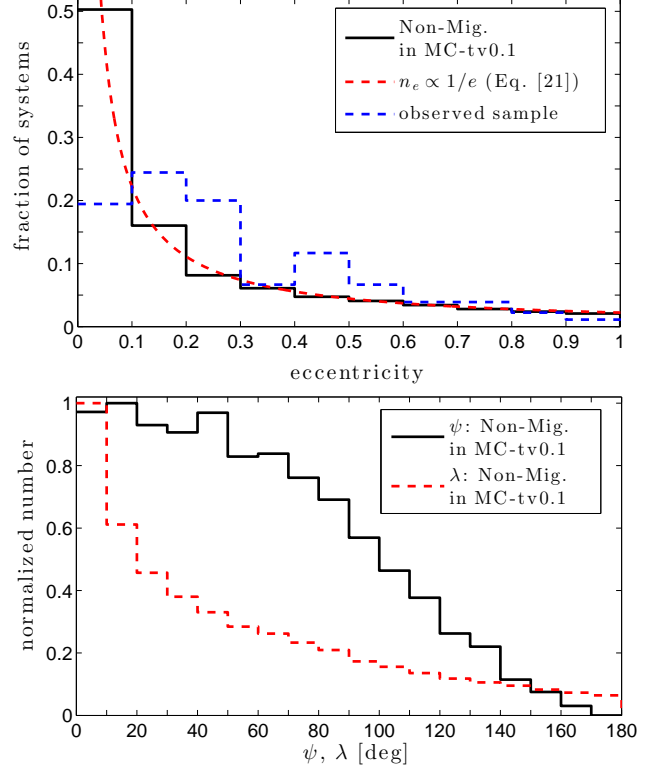


FIG. 11.— Final eccentricity distribution (upper panel) and final obliquity distribution (lower panel) for the non-migrating planets in MC-tv0.1. *Upper panel:* the analytic time-averaged distribution (red dashed line) from Equation (21), normalized so it coincides with the center of the first bin in the simulation, and the observed sample (blue dashed line) of 180 RV-detected planets with  $M \sin i > 0.1 M_J$ ,  $a > 1$  AU, and no detected planetary companions. *Lower panel:* stellar obliquity  $\psi$  and projected stellar obliquity  $\lambda$  (normalized by the tallest bin).

in our simulations, our results are consistent with the steady-state flow of migrating planets given by Socrates et al. (2012a). Since KL migration happens either fast compared to the planet lifetime or slow but spending a small fraction of the time in the migration track with  $a < 2$  AU, our simulations form  $\sim 3$  highly eccentric planet and 1 moderately eccentric HJ for every  $\sim 300$  HJs in circular orbits. This result is consistent with lack of highly eccentric planets at intermediate periods seen in *Kepler* (Dawson et al. 2012), but is inconsistent with the number of moderately eccentric HJs in the RV sample and, therefore, with the expected number of highly eccentric planets in *Kepler* predicted by Socrates et al. (2012a).

## 9. NON-MIGRATING PLANETS

From Table 1 we observe that the fraction of non-migrating planets ( $a > 4.5$  AU) in all the simulations is  $\sim 70 - 90\%$  or  $\sim 8 - 50$  non-migrating planets for every HJ formed, which is roughly consistent with the ratio of  $\sim 10 - 16$  between the number of giant planets at  $a > 1$  AU and the number of HJs derived from RV surveys (see §7.2). Here, we show the steady-state eccentricity and obliquity distributions of these planets, which can potentially be compared with the observed giant planets at a few AU.

In Equation (B7), we calculate the time-averaged ec-

centricity distribution over a KL cycle  $n_e(e_{\text{in}}|i_0)$  for a planet that starts with  $e^2 \ll 1$ , where the perturber has an inclination  $i_0$ . In this limit, an isotropic distribution of perturbers produces a population of planets with a time-averaged eccentricity distribution given by

$$n_e(e) \propto \int \frac{d \cos i_0}{e \left[ \frac{3}{5}(1 - e^2) - \cos^2 i_0 \right]^{1/2}} \propto \frac{1}{e}, \quad (21)$$

where the integral is taken over  $\cos^2 i_0 < \frac{3}{5}(1 - e^2)$  and the eccentricity has lower bound, say  $e > 0.01$ , otherwise  $n_e(e)$  diverges (the eccentricity remains small for an arbitrarily large fraction of the KL cycle as  $e \rightarrow 0$ ).

In the upper panel of Figure 11, we show the eccentricity distribution of the non-migrating planets in our fiducial simulation MC-tv0.1 and the time-averaged distribution from Equation (21). We observe that the distributions coincide, which indicates that the modulation from the octupole-level gravitational interactions (ignored in the analytic derivation) do not play a significant role at shaping the steady-state eccentricity distribution. Recall from §4.3 that the octupole-level interactions do play a major role at producing extremely high eccentricities and, therefore, HJs and tidal disruptions.

In Figure 11, we compare this eccentricity distribution with that from a sample of planets detected in RV surveys with no detected planetary companions. We observe that the KL mechanism overproduces systems with low eccentricities (mean and median of  $\simeq 0.2$  and  $\simeq 0.1$ ), while it produces too few systems with intermediate eccentricities ( $e \sim 0.1 - 0.3$  and  $e \sim 0.4 - 0.6$ ) relative to the observations. This is in agreement with the previous numerical work by Takeda & Rasio (2005) who find that the KL mechanism leaves roughly  $\sim 50\%$  of the systems with  $e \lesssim 0.1$  and produces a deficit of planets with  $e \simeq 0.1 - 0.6$  relative to the observations. Contrary to Takeda & Rasio (2005), we do not find that the KL mechanism produces an excess of planets with  $e > 0.6$  (except for the  $0.9 - 1$  bin in which the difference is not statistically significant). This difference might be due to the different observed sample considered by these authors (72 RV planets with  $a > 0.1$  AU excluding multiple-planet systems) and the fact that in our simulations the planets can migrate and get disrupted, which would tend to remove planets with the highest eccentricities.

In the lower panel of Figure 11, we show the obliquity  $\psi$  and the projected obliquity  $\lambda$  distribution of the non-migrating planets. Note that even in the absence of KL oscillations the obliquity evolves due to the planetary nodal precession caused by an inclined companion. The mean and median values of  $\psi$  ( $\lambda$ ) are  $\simeq 58^\circ$  ( $\simeq 52^\circ$ ) and  $\simeq 53^\circ$  ( $\simeq 38^\circ$ ), respectively.

We conclude that the eccentricity distribution of the non-migrating planets follows the simple expression derived in Appendix B and differs from the observed distribution of planets at a few AU because the KL mechanism produces too many (few) planets with  $e \lesssim 0.1$  ( $e \sim 0.1 - 0.6$ ) relative to the observations. Also, these planets have a wide distribution of stellar obliquities.

## 10. DISCUSSION

The main result from our study is that Kozai-Lidov migration in stellar binaries produces Hot Jupiters with a semi-major axis distribution that is shifted towards low

values compared to the observations.

We show (Figure 7) that the dominant migration channel is “fast” KL migration (as opposed to “slow” KL migration; see description of these regimes in §2-3). This result implies that planets migrate preferentially to small ( $a < 0.03$  AU) semi-major axis (see Eq. [11]), where the observed sample contains only  $\sim 3\%$  and  $\simeq 9\%$  of HJs detected in RV and transit surveys, respectively. The tidal disruption distance sets the minimum semi-major axis attainable by a fast-migrating HJ. As a result, the final semi-major axis distribution of the HJs formed in our Monte Carlo simulations (see Figure 4) shows a significant pile-up of planets at roughly twice the tidal disruption distance ( $R_t$  in Eq. [14]).

In contrast, the subdominant slow KL migration channel is responsible for the HJs with large ( $0.05$  AU  $\lesssim a \lesssim 0.1$  AU) semi-major axes, where the observed sample contains  $\simeq 46\%$  and  $\simeq 45\%$  of the observed HJ population detected in RV and transit surveys, respectively. In §2.1 we show that the “bottleneck” that limits the production of such HJs is the phase in which the planet is undergoing KL oscillations at a few AU, which constrains the minimum amount of tidal dissipation required to form these planets (Eq. [10]). From our simulations (upper panel of Figure 6) and analytical estimates we get a lower limit to the amount of tidal dissipation in the planet of  $t_{V,2} < 0.1$  yr (or a time lag  $\tau_2 > 9$  s) for a Jupiter-like planet.

A way to bring the results into better agreement with the observed semi-major axis distribution is to limit the production of HJs with the shortest periods. One can achieve this in our model by either

- setting the tidal disruption distance at large enough values,  $f_t \simeq 3.2 - 3.6$  in  $R_t$  from Equation (14) is preferred by the data, or
- considering that Jupiter-like planet starts inflated with a radius of  $\sim 1.5 - 2R_J$  and then shrink to  $R_J$ , as we show in §5.3.

Note that the most recent calculations of the tidal disruption distance in Jupiter-like planets by Guillochon et al. (2011); Liu et al. (2012) result in  $f_t \simeq 2.7$ , which according to these authors might be regarded as a lower limit since disruptions can still happen at wider separations from repeated pericenter passages.

Planetary cooling models predict that Jupiter-like planets are born with larger radii and shrink in timescales of  $\sim 10^7$  yr (e.g., Burrows et al. 1997). Gas giant planets can also be inflated due to energy dissipation during migration (e.g., Gu et al. 2003), which can also limit the formation of the shortest-period planets. We ignore this effect in our simulations and discuss its possible consequences in §10.2.2.

Evidently, limiting the production of the shortest-period planets comes at the expense of significantly reducing the overall efficiency of KL migration to produce HJs (see Figure 5).

The overall rate of HJ production derived from our simulations is  $\sim 2 - 7\%$  per binary systems harboring a giant planets at a few AU (Table 1). As discussed in §7.2, the previous rate can account for  $\simeq 3 - 23\%$  of the Hot Jupiter population based on the planets discovered in RV surveys.

In §7.1, we compare the semi-major axis distribution from our simulations and the observed sample, and find that KL migration accounts for at most  $\sim 20\%$  ( $\sim 40\%$ ) based on the planets discovered in transit surveys and corrected by a detection probability  $\propto a^{-5/2}$  ( $\propto a^{-1}$ , the geometric bias). This fraction ignores the simulations in which the planetary radii varies in time (Rp-tv0.1 and Rp-tv0.01) in which case the fraction rises to  $\sim 40\%$  ( $\sim 70\%$ ).

By simultaneously using the constraint from occurrence rate and the semi-major axis distribution of HJs (Table 2), we find that the simulation that can produce the highest fraction of the observed HJs is MC-tv0.01 with a contribution of at most  $\simeq 23\%$ .

Other results from our Monte Carlo simulations include:

1. The stellar obliquity angle distribution is significantly flatter in  $\psi \simeq 0^\circ - 140^\circ$  than that obtained from simulations with quadrupole-level gravitational interactions only ( $\epsilon_{\text{oct}} = 0$  in Eq. [A3]) and the distribution is fairly insensitive to the amount of tidal dissipation and the tidal disruption distance. The theoretical distribution fails to describe the observations because it produces too many misaligned planets, while a large fraction of the observations have projected obliquities  $\lambda < 30^\circ$ . This result places a crude upper limit of  $\sim 50\%$  to the contribution from KL migration to the observed obliquity distribution. By considering the simulation with  $\epsilon_{\text{oct}} = 0$  or with shorter initial host stars spin periods the distribution compares better with the observations (see panel d of Figure 8).

Note that the disagreement between our simulations and the observations does not pose a major problem for our model since we find that KL migration might only account for up to  $\sim 20\%$  of HJs, as discussed above. Also, as shown by Morton & Johnson (2011) and Naoz et al. (2012) the obliquity distribution might be explained by a population of misaligned systems from KL migration and/or planet-planet scattering plus a population of aligned systems from disk-migration (or secular interactions of nearly coplanar planets proposed by Petrovich 2014). Moreover, the observed distribution of misalignments might be sculpted by tides in the star and this would difficult the comparison between our models and the observations (Dawson 2014).

2. KL migration produces too few intermediate period planets ( $0.1 \text{ AU} < a < 2 \text{ AU}$ ): roughly  $\sim 1$  intermediate period planet for every  $\sim 50 - 200$  HJs. As discussed in §8, this is due to the prevalence of fast KL migration and also due to nature of slow KL migration where migrating planets spend most of their lifetimes undergoing KL oscillations or as a HJ in a low-eccentricity orbit. This result is consistent with the lack of intermediate period planets found in *Kepler* (Dawson et al. 2012), however, the predictions might be sensitive to the details of tidal dissipation in the planet at very high eccentricities (see discussion in §10.2.3).

3. KL migration produces a large population of non-migrating planets ( $\sim 70\%$  of the simulated systems) with an eccentricity distribution that can be well-described by the analytic distribution  $n_e \propto 1/e$  (see Appendix B). Such distribution produces an excess (deficit) of planets with  $e < 0.1$  ( $e \sim 0.1 - 0.6$ ) relative to the observations, as previously found by Takeda & Rasio (2005). Contrary to the results of these authors, we do not find that the KL mechanism produces a significant excess of planets in very eccentric orbits relative to the observations.

#### 10.1. Relation to previous work on KL migration

The first studies of planetary KL migration in ensembles of stellar binary systems are those by Wu et al. (2007) and Fabrycky & Tremaine (2007).

Fabrycky & Tremaine (2007) describe the distribution of spin-orbit misalignment angles from KL migration by considering an isotropic distribution of stellar perturbers with fixed eccentricity  $e_{\text{out}} = 0$  and semi-major axis  $a_{\text{out}} = 500 \text{ AU}$  (identical to our simulation SMA500e0). Such distribution can roughly describe the observed obliquity distribution of Hot Jupiters (panel d Figure 8). However, the eccentricity and semi-major axis distributions of stellar binaries are wide and as shown by Naoz et al. (2012) the higher-order terms in the gravitational potential can significantly modify the obliquity distribution (see panel a of Figure 8).

Similarly, Wu et al. (2007) studied the KL migration based on an observationally-motivated distribution of binary eccentricities and semi-major axes. These authors predicted that KL migration can produce HJs in  $\simeq 2.5\%$  of their simulations. However, they ignored the effect from the octupole-level gravitational interactions, which according to Naoz et al. (2012) increases the formation rate of HJs in the simulations up to  $\sim 15\%$ . As we show here, such high efficiency of forming HJs in Naoz et al. (2012) is due to the small tidal disruption distance used in their simulations ( $f_t = 1.66$  in Eq. [14]). The formation rate is a steep function of the disruption distance and by decreasing the disruption distance, the formation rate can be as high as  $\sim 26\%$  (Figure 5). Using our fiducial disruption distance ( $f_t = 2.7$  in Eq. [14]) we find that our simulations produce HJs in only  $\simeq 1.5 - 7.4\%$  of our simulations.

Unlike Naoz et al. (2012), we have studied the semi-major axis distribution of HJs from KL migration. This has allowed us to place constraints that are complementary to those provided by the formation rate because the semi-major axis distribution, unlike the obliquity distribution, is very sensitive to the disruption distance. Wu et al. (2007) did study the semi-major axis distribution and showed that KL migration in binaries can reproduce the observed semi-major axis distribution when the simulation starts with an inflated planet, which then shrinks (similar to our simulation Rp-tv0.03). However, their study ignores the effect from the octupole in the gravitational interactions, which, as we show here, is important to describe the semi-major axis distribution of HJs because it gives rise to the strong pile-up at twice the disruption distance. Recall that we observed that  $\sim 20 - 30\%$  our simulations have disruptions, while the simulations by Wu et al. (2007) had none.

Different from all these previous works, we have stud-

ied the orbital distribution of planetary systems due to KL migration, focusing not only on the formation of HJs but also on the expected distributions of planets at wider separations: the intermediate period planets and non-migrating planets.

More recently, Martí & Beaugé (2014) studied the formation of HJs due to KL migration in stellar binaries. The orbital elements of the binary systems result from stellar scattering from a third star. The authors claim that the 3-day pile-up is a natural outcome from tidal trapping (roughly equivalent to fast migration in our formalism) from quasi-parabolic orbits. We observe, however, that their simulations produce HJs that have not yet circularized for  $a \gtrsim 0.03$  AU and are still on the migration track  $a(1 - e^2) \simeq 0.03$  AU. Thus, the formation of HJs at  $a \gtrsim 0.04$  AU is at the expense of eccentric planets that have not finished migration. However, based in either the RV or the transit sample, the observed semi-major axis distribution is centered around  $\simeq 0.04 - 0.06$  AU (see §5) and most ( $\gtrsim 95\%$ ) of these planets have small eccentricities ( $e < 0.2$ ).

The major difference between the simulations by Martí & Beaugé (2014) and this work is given by the prescription for tidal dissipation. In our work, we have used the equilibrium tide model for the whole evolution, while Martí & Beaugé (2014) implement a recipe to describe the effect of dynamical tides calculations by Ivanov & Papaloizou (2011) at high eccentricities ( $e > 0.9$ ) and the equilibrium tides at smaller eccentricities. The main consequence of doing this is that migration slows down considerably when equilibrium tides take over and, therefore, many planets appear to be still in the migration track compared to our simulations.

### 10.2. Effects ignored in our simulations

In what follows we describe extra effects that have been ignored in our simulations and how these could change our results.

#### 10.2.1. Orbital evolution of Hot Jupiters due to tidal dissipation in the host star

Once a Hot Jupiter in a circular orbit has formed in our simulations, the planet rotates synchronously with the orbital frequency and there is essentially no subsequent orbital evolution due to tides raised in the planet. However, tides raised in the host star can still lead to evolution of the Hot Jupiter.

The characteristic evolution timescale of the spin host star and the orbit of the Hot Jupiter is roughly given by the tidal friction timescale<sup>14</sup>. From Equation (A16), we get

$$t_{F,1} \simeq 15 \text{ Gyr} \left( \frac{t_{V,1}}{50 \text{ yr}} \right) \left( \frac{a}{0.03 \text{ AU}} \right)^8 \left( \frac{R_\odot}{R_1} \right)^8 \times \left( \frac{M_1}{M_\odot} \right) \left( \frac{M_J}{M_2} \right), \quad (22)$$

where  $t_{V,1}$  is the viscous time of the host star. For the parameters in Equation (22), the tidal friction timescale is equivalent to that calculated using a quality factor of

<sup>14</sup> Note that the orbital decay timescale is shorter than the tidal friction timescale due to the strong dependence of the tidal friction timescale on  $a$ .

$Q \simeq 3 \times 10^5$  for a Hot Jupiter at  $a = 0.03$  AU. Note that such value of  $Q$  is typically low compared to the theoretical values of  $\sim 10^6 - 10^7$  (see references in Lai 2012) and the tidal friction timescale is likely to be longer than that in Equation (22).

From Equation (22) we see that tidal dissipation in the host star might have little effect on the host star spin<sup>15</sup> and the orbit of the Hot Jupiter (e.g.,  $\psi$  and  $a$ ) if these planets are formed at  $a \gtrsim 0.03$  AU (although see Lai 2012). On the contrary, for Hot Jupiters closer-in ( $a \lesssim 0.03$  AU) tides can in principle change the values of  $\psi$  and  $a$  we derive in our simulations. Recent calculations by Valsecchi & Rasio (2014a,b) show that the obliquity and semi-major axis of observed HJ systems can evolve significantly. In particular, systems that lie within twice the Roche limit ( $a < 2R_t$  with  $f_t = 2.16$  in Eq. [14]) might have spiraled in from an initial semi-major axis that is larger than twice the Roche limit (Valsecchi & Rasio 2014b).

The host star's spin period in Hot Jupiter systems is typically larger than the orbital period so the orbit would decay in most cases. In principle, this effect can limit the production of planets with small semi-major (e.g., Levrard et al. 2009; Jackson et al. 2009) and change the obliquity distribution. Note that the obliquity of Hot Jupiter systems is expected to decrease for prograde orbits ( $\psi < 90^\circ$ ), while it can either increase or decrease for retrograde orbits ( $\psi > 90^\circ$ ) depending on the ratio of the orbital and the spin angular momenta. As shown by Rogers & Lin (2013), the retrograde HJs would typically evolve towards  $180^\circ$  and, therefore, the subsequent tidal dissipation in the star is not expected to bring our results for the obliquity distribution in better agreement with the observations. Finally, this re-alignment process might be more efficient in HJs orbiting cooler stars than hot star and could, in principle, account for the observed trend of obliquity with surface temperature (e.g., Albrecht et al. 2012).

We conclude that the semi-major axis distribution of Hot Jupiters formed in our simulations is expected to change only slightly by subsequent tidal dissipation with the host star because such planets are formed with large enough semi-major axis. However, if these planets do experience some orbital decay our predicted semi-major distribution would evolve towards lower values making our results stronger. Also, the obliquity distribution might evolve but is not expected to bring the results in better agreement with the observations because we expect that most retrograde planets will evolve towards  $180^\circ$ .

#### 10.2.2. Planetary inflation

During KL migration the orbital energy dissipated is about  $\sim 10$  times ( $\sim R_J/a_f \cdot M_\odot/M_J$  with  $a_f$  the final semi-major axis) planet's binding energy, while the tidal dissipation rate in the planet is expected to exceed that in the host star (compare  $t_{F,1}$  and  $t_{F,2}$  in Eq. [A16]). Provided that this orbital energy is deposited deep enough in the planet (not immediately radiated away), the planet might be subject to inflation due to tidal heating (Bodenheimer et al. 2001, 2003; Gu et al. 2003).

<sup>15</sup> Assuming a solar-type star with spin period of  $\sim 1 - 10$  days.

Given the strong dependence of the tidal dissipation rate on the planet ( $1/t_{F,2} \propto R_2^8$  in Eq. [A16]), planetary inflation can substantially speed up the migration, while at the same time the inflated planet is more susceptible to being tidally disrupted. This scenario is similar to our case in which the planets initially have a larger radii and then shrink (see discussion in §5.3), expect that for tidally inflated planets the change in radius depends on the orbital evolution and details of tidal dissipation.

Based on simulations with a time-varying planetary radius (Rp-tv0.1 and Rp-tv0.01), we expect that planetary inflation would limit the production of HJs with small semi-major axes ( $a < 0.03$  AU): such planets would be more susceptible to tidal disruptions because these HJs reach the smallest pericenter distances during migration, which would inflate the planet more efficiently and increase the tidal disruption distance ( $R_t$  in Eq. [14]). Moreover, such short-period HJs might also be subject to mass loss episodes in which case the planet would migrate outwards as a result of total angular momentum conservation (Gu et al. 2003).

We conclude that considering planetary inflation in our models would shift the semi-major axis distribution to larger values in better agreement with the observations, similar to our models in which the planet is initially inflated.

### 10.2.3. Effect from dynamical tides

The tidal distortion in planets at very high eccentricities is generated only at the pericenter and is negligible during the rest of the orbit so the planet can no longer achieve equilibrium figures as described in the equilibrium tide model (Hut 1981). Instead, the energy deposited in normal modes (surface gravity waves) during a periastron passage can be dissipated and lead to orbital decay, which is described in the dynamical tide model (e.g., Lai 1997; Ivanov & Papaloizou 2005). We have ignored the effect from dynamical tides in our simulations.

Most importantly for our study, the model of dynamical tides by Ivanov & Papaloizou (2011) predicts migration timescales that depend more steeply (exponentially) on the pericenter distance than the equilibrium tides from Hut (1981), which predict a migration timescale  $\tau_a \propto [a(1-e)]^{15/2}$  (Eq. [5]).

Beaugé & Nesvorný (2012) use a recipe for tidal dissipation that attempts to describe the effect of dynamical tides in the migration rates at high eccentricities using the calculations by Ivanov & Papaloizou (2011) and the equilibrium tide approximation we have used in this work. To do so, the authors added an empirical correction factor to the migration timescale from the constant time-lag model of  $10^{200e^2(a(1-e)-0.022\text{AU})}$ , which has a significant effect only at high eccentricities. This prescription enhances the migration rate when the pericenter distance is  $< 0.022$  AU, while it slows it down for  $> 0.022$  AU (the specific change-over distance of 0.022 AU changes only slightly depending on the planetary viscous times or time-lag).

Based on this description of tidal dissipation in the planet at high eccentricities, we expect the following effects in our calculations:

- the formation of HJs with small semi-major axes ( $a < 0.03$  AU) should increase because these plan-

ets result from tidal circularization of highly eccentric orbits with pericenter distances  $a(1-e) < 0.015$  AU, which are expected to migrate at least  $\sim 25$  times more rapidly than in our calculations according to the prescription by Beaugé & Nesvorný (2012). Additionally, this effect would allow many planets to migrate fast enough so that they are not tidally disrupted, implying that the number of HJs increases at the expense of having less tidally disrupted planets.

- the formation of HJs with large semi-major axis ( $a > 0.05$  AU) should decrease relative to our simulations because these planets are formed by slow KL migration in which high-eccentricity orbits reach pericenter distances of  $a(1-e) \gtrsim 0.025$  AU and, therefore, the migration timescale is expected to be longer in the model by Ivanov & Papaloizou (2011).
- the number of intermediate period planets and eccentric HJs should increase because a large fraction of fast-migrating planets would slow-down their migration as their orbits circularize and enter the regime in which equilibrium tides takes over.

From these speculative arguments we conclude that that the model dynamical tides by Ivanov & Papaloizou (2011) would produce a semi-major axis distribution of the HJs skewed towards lower values compared to our simulations. This result would strengthen our main result that KL migration produces too many HJs with small semi-major axis relative to the observations.

### 10.2.4. The validity of the secular approximation

We have approximated the dynamical evolution of the three-body system using double-orbit averaging. Using direct  $N$ -body integrations, Antognini et al. (2014) showed that this approximation might break down for  $(a_{\text{out}}/a_{\text{in}})(m_1 + m_2)/m_3 \simeq 20$  or lower values (see also Antonini et al. 2014). In this regime, the authors observe that once the planet reaches very high eccentricities in a KL cycle, extra eccentricity oscillations occur with timescale given by the period of the outer body (Ivanov et al. 2005).

The eccentricity reached due to these extra oscillations seen in the  $N$ -body calculations is larger than that obtained from the double-averaging calculations (Antognini et al. 2014). Also, the timescale of such oscillations is shorter than the KL timescale by factor  $\sim P_{\text{in}}/P_{\text{out}}$  and this short-period eccentricity forcing can more easily overcome the effect of tidal damping and precession of the pericenter from GR.

The previous observations have a few consequences for our work. First, the number of tidally disrupted planets is expected to increase and the HJ period distribution would shift to lower values. This would strengthen our result that KL migration produces a semi-major axis distribution skewed towards low values relative to the observations. Second, short-period changes to the eccentricity can promote migration of systems that do not reach high enough eccentricities in the double-averaging approximation. This effect should not change our results because we observe that migration happens for perturbors typically at  $a_{\text{out}} > 250$  AU (Figure 3, panel d) and, therefore,

$(m_1 + m_2)/m_3(a_{\text{out}}/a_{\text{in}}) > 50$ , where double averaging is expected to be a good approximation (Ivanov et al. 2005).

#### 10.2.5. Fate of tidally disrupted planets

We have shown that  $\sim 20 - 25\%$  of the planets in our Monte Carlo simulations are tidally disrupted (see Table 1). The overall rate can be estimated as in §7.2 and results in  $\sim 1\%$  of the solar-type stars having a tidal disruption event. This is a lower limit because we limit our study to wide binaries ( $a_{\text{out}} > 100$  AU), while both the rate of disruptions in the simulations and the binary fraction increase for tighter binaries. Additionally, the rate of disruptions can be enhanced even further if we were to start with planets in highly eccentric orbits and in low inclination binaries (Li et al. 2014).

From panels (a) and (c) in Figure 3 we observe that planets get disrupted on very eccentric orbits ( $e > 0.99$ ) at  $a > 2$  AU. Also, the distribution of stellar obliquities in our fiducial simulation at the moment of disruption (not shown) span the range  $\psi = 0^\circ - 170^\circ$ , while the median is  $\simeq 70^\circ$  and most systems ( $\simeq 75\%$ ) are disrupted in prograde orbits ( $\psi < 90^\circ$ ).

For a Jupiter-like planet orbiting a solar mass host star at  $a > 2$  AU the orbital energy is  $> 15$  times smaller than its self-binding energy. According to Guillochon et al. (2011), a Jupiter-like planet crossing the disruption distance ( $R_t$  in Eq. [14] with  $f_t = 2.7$ ) at these separations loses slightly less than half of its initial mass which ends up being accreted by the host star, while the stripped planet gets ejected from the system. The gas falls into the host star through an accretion disk that emits optical and UV radiation for  $\sim$  days to a year with a peak luminosity of  $10^{36} - 10^{37} \text{ erg s}^{-1}$  (Metzger et al. 2012). Also, the gas lost by the planet can have enough angular momentum to significantly alter the spin rate of the host star and even its axis of rotation.

We conclude that given the large number of planetary disruptions, KL migration might contribute to the population of free-floating planets by the ejection of planetary cores after gas stripping, while the gas that remains bounded to the host star might provide a significant source of transient radiation.

### 11. SUMMARY

We study the steady-state orbital distributions of giant planets migrating through the combination of the Kozai-Lidov (KL) mechanism due to a stellar companion and friction due to tides raised on the planet by the host star.

We find that KL migration cannot produce all Hot Jupiters (HJs). It can, however, produce a fraction constrained by the following observations:

1. The observed semi-major axis distribution is consistent with KL migration (simulation Rp-tv0.03) if the following are both true:
  - a lower limit to the amount of tidal dissipation in the planet, parametrized by the planetary viscous time, is:  $t_{V,2} < 0.1$  yr. Otherwise, KL migration is unable to produce HJs in the semi-major axis range  $0.05 \text{ AU} \lesssim a \lesssim 0.1 \text{ AU}$ , which contains  $\simeq 46\%$  ( $\simeq 45\%$ ) of the observed HJ population detected in RV (transit)

surveys. This lower limit to the amount of dissipation is larger by a factor of  $\simeq 150$  than the upper limit inferred from the Jupiter-Io interaction of  $t_{V,2} > 15$  yr.

- the distance at which a Jupiter-like planet in a highly eccentric orbit gets tidally disrupted is  $\gtrsim 0.015$  AU. Otherwise, too many planets migrate to  $a < 0.03$  AU, where the observed sample contains only  $\sim 3\%$  ( $\simeq 9\%$ ) of HJs detected in RV (transit) surveys. One can achieve this large disruption distance either by setting  $f_t \gtrsim 3.2$  in Equation (14) for a Jupiter-like planet or by starting with an inflated planet, which then shrinks as in §5.3. In principle, the tidal dissipation in the star can also prevent the formation of short-period planets.

If the standard parameters are used ( $f_t \simeq 2.7$  and no radius shrinkage), KL migration can produce at most  $\sim 20 - 40\%$  of the Hot Jupiters.

2. The observed occurrence rate of HJs is roughly consistent with KL migration if  $f_t \lesssim 1$  (almost no tidal disruptions take place). If our fiducial disruption distance ( $f_t \simeq 2.7$ ) is used, KL migration produces HJs at a rate which is only  $\sim 3 - 20\%$  of the observed one.
3. The distribution of the stellar obliquity angles of HJs is inconsistent with KL migration. This distribution is fairly insensitive to the amount of tidal dissipation and disruption distances in our simulations. Based on the fraction of misaligned planets in the observations, KL migration can produce at most  $\sim 50\%$  of the HJs, independent of  $t_{V,2}$  and  $f_t$ . Better agreement with the data is found when the host star's spin period is initially shorter.

By simultaneously considering the constraints from the occurrence rate and the semi-major axis distribution above, we find a maximum fraction of  $\sim 20\%$  of the Hot Jupiters can be formed by KL migration due to binaries (simulation MC-tv0.01).

Additionally, KL migration in binaries is unable to form intermediate-period planets ( $0.1 \text{ AU} \lesssim a \lesssim 2 \text{ AU}$ ) because migrating planets spend most of their lifetimes undergoing KL oscillations at  $a > 2$  AU or as a Hot Jupiter at  $a < 0.1$  AU.

I acknowledge support from the CONICYT Bicentennial Becas Chile fellowship. I am indebted to Scott Tremaine who has critically and patiently read and commented on various versions of this paper. I am also grateful to Rebekah Dawson, Subo Dong, Chelsea Huang, Boaz Katz, Renu Malhotra, Tim Morton, and Smadar Naoz, for enlightening discussions and comments. I gratefully acknowledge an anonymous referee for constructive feedback. All simulations were carried out using computers supported by the Princeton Institute of Computational Science and Engineering.

## APPENDIX

## EQUATIONS OF MOTION

We explicitly show the secular equations of motion for a hierarchical triple system considering gravitational interactions up to the octupole approximation (i.e., expanding the gravitational interactions between the inner and outer binaries up to  $a_{\text{in}}^3/a_{\text{out}}^4$ ). We do not assume the total mass or angular momentum is in two of the bodies. We also include the non-Keplerian effects and tidal dissipation relevant to our problem.

We define the inner orbit relative to the center of mass of bodies 1 and 2, while the outer orbit is defined relative to the center of mass of bodies 3 and the center of mass of bodies 1 and 2. We specify the orientation of the inner and outer orbits by their Laplace-Runge-Lenz vectors  $\mathbf{e}_{\text{in}}$  and  $\mathbf{e}_{\text{out}}$ , whose magnitudes are  $e_{\text{in}}$  and  $e_{\text{out}}$ . Similarly, we express the angular momentum vectors as

$$\mathbf{h}_{\text{in}} = \frac{m_1 m_2 \sqrt{G(m_1 + m_2) a_{\text{in}} (1 - e_{\text{in}}^2)}}{(m_1 + m_2)} \hat{\mathbf{h}}_{\text{in}} \quad (\text{A1})$$

$$\mathbf{h}_{\text{out}} = \frac{(m_1 + m_2) m_3 \sqrt{G(m_1 + m_2 + m_3) a_{\text{out}} (1 - e_{\text{out}}^2)}}{(m_1 + m_2 + m_3)} \hat{\mathbf{h}}_{\text{out}}, \quad (\text{A2})$$

and by defining the vectors  $\hat{\mathbf{q}}_{\text{in}} = \hat{\mathbf{h}}_{\text{in}} \times \hat{\mathbf{e}}_{\text{in}}$  and  $\hat{\mathbf{q}}_{\text{out}} = \hat{\mathbf{h}}_{\text{out}} \times \hat{\mathbf{e}}_{\text{out}}$  we complete the right-hand triad of unit vectors  $(\hat{\mathbf{q}}_{\text{in}}, \hat{\mathbf{h}}_{\text{in}}, \hat{\mathbf{e}}_{\text{in}})$  and  $(\hat{\mathbf{q}}_{\text{out}}, \hat{\mathbf{h}}_{\text{out}}, \hat{\mathbf{e}}_{\text{out}})$ . In our notation, the sub-index 1 indicates the host star, 2 the planet, and 3 the outer perturber.

The double time averaging of the perturbing potential over the orbital periods of the inner and outer orbits yields (e.g., Farago & Laskar 2010; Correia et al. 2011; Tremaine & Yavetz 2014)

$$\begin{aligned} \phi_{\text{oct}} = & \frac{\phi_0}{(1 - e_{\text{out}}^2)^{3/2}} \left[ \frac{1}{2} (1 - e_{\text{in}}^2) (\hat{\mathbf{h}}_{\text{in}} \cdot \hat{\mathbf{h}}_{\text{out}})^2 + \left( e_{\text{in}}^2 - \frac{1}{6} \right) - \frac{5}{2} (\mathbf{e}_{\text{in}} \cdot \hat{\mathbf{h}}_{\text{out}})^2 \right] + \\ & + \frac{\epsilon_{\text{oct}} \phi_0}{(1 - e_{\text{out}}^2)^{3/2}} \left\{ (\mathbf{e}_{\text{in}} \cdot \hat{\mathbf{e}}_{\text{out}}) \left[ \left( \frac{1}{5} - \frac{8}{5} e_{\text{in}}^2 \right) - (1 - e_{\text{in}}^2) (\hat{\mathbf{h}}_{\text{in}} \cdot \hat{\mathbf{h}}_{\text{out}})^2 + 7 (\mathbf{e}_{\text{in}} \cdot \hat{\mathbf{h}}_{\text{out}})^2 \right] + \right. \\ & \left. - 2 (1 - e_{\text{in}}^2) (\hat{\mathbf{h}}_{\text{in}} \cdot \hat{\mathbf{h}}_{\text{out}}) (\mathbf{e}_{\text{in}} \cdot \hat{\mathbf{h}}_{\text{out}}) (\hat{\mathbf{h}}_{\text{in}} \cdot \hat{\mathbf{e}}_{\text{out}}) \right\}, \\ \text{where } \phi_0 = & \frac{3G}{4} \frac{a_{\text{in}}^2}{a_{\text{out}}^3} \frac{m_1 m_2 m_3}{m_1 + m_2}, \quad \epsilon_{\text{oct}} = \frac{25}{16} \frac{a_{\text{in}}}{a_{\text{out}}} \frac{e_{\text{out}}}{(1 - e_{\text{out}}^2)} \frac{m_1 - m_2}{m_1 + m_2}. \end{aligned} \quad (\text{A3})$$

This potential reduces to that given by Katz, Dong, & Malhotra (2011) in the test particle limit ( $m_2 \ll m_1, m_3$ ) when one fixes the outer perturber's orbit to  $\mathbf{h}_{\text{out}} = h_{\text{out}} \hat{\mathbf{z}}$  and  $\mathbf{e}_{\text{out}} = e_{\text{out}} \hat{\mathbf{x}}$ . A similar expression can be found in Ford et al. (2000) and Naoz et al. (2013a), but in terms of orbital elements rather than the eccentricity and angular momentum vectors.

By following Tremaine et al. (2009) one can easily write the equations of motion for the eccentricity and angular momentum vectors by taking gradients of the potential. These fully describe the secular evolution of the inner and outer orbits when only the gravitational interactions are taken into account. The advantage of this procedure is that the equations of motion derived from  $\phi_{\text{oct}}$  do not diverge as the inner orbit approaches radial ( $e_{\text{in}} \rightarrow 1$ ) and circular orbits ( $e_{\text{in}} \rightarrow 0$ ) as happens when using the equations of motion in terms of the orbital elements (Ford et al. 2000; Naoz et al. 2013a).

The full set of equations describing the secular gravitational interaction, precession from general relativity, stellar oblateness, tidal friction, and the rotation of the star and inner planet can be written in a similar way as in Eggleton & Kiseleva-Eggleton (2001) as:

$$\begin{aligned} \frac{d\mathbf{e}_{\text{in}}}{dt} = & (Z_1 + Z_2 + Z_{\text{GR}}) e_{\text{in}} \hat{\mathbf{q}}_{\text{in}} - (Y_1 + Y_2) e_{\text{in}} \hat{\mathbf{h}}_{\text{in}} - (V_1 + V_2) \mathbf{e}_{\text{in}} \\ & + \tau_{\text{in}}^{-1} \left[ (1 - e_{\text{in}}^2)^{1/2} \hat{\mathbf{h}}_{\text{in}} \times \nabla_{\mathbf{e}_{\text{in}}} \tilde{\phi}_{\text{oct}} + \mathbf{e}_{\text{in}} \times \nabla_{h_{\text{in}}} \tilde{\phi}_{\text{oct}} \right], \end{aligned} \quad (\text{A4})$$

$$\begin{aligned} \frac{1}{h_{\text{in}}} \frac{d\mathbf{h}_{\text{in}}}{dt} = & (Y_1 + Y_2) \hat{\mathbf{e}}_{\text{in}} - (X_1 + X_2) \hat{\mathbf{q}}_{\text{in}} - (W_1 + W_2) \hat{\mathbf{h}}_{\text{in}} \\ & + (1 - e_{\text{in}}^2)^{-1/2} \tau_{\text{in}}^{-1} \left[ \mathbf{e}_{\text{in}} \times \nabla_{\mathbf{e}_{\text{in}}} \tilde{\phi}_{\text{oct}} + (1 - e_{\text{in}}^2)^{1/2} \hat{\mathbf{h}}_{\text{in}} \times \nabla_{h_{\text{in}}} \tilde{\phi}_{\text{oct}} \right], \end{aligned} \quad (\text{A5})$$

$$\frac{d\mathbf{e}_{\text{out}}}{dt} = \tau_{\text{out}}^{-1} \left[ (1 - e_{\text{out}}^2)^{1/2} \hat{\mathbf{h}}_{\text{out}} \times \nabla_{\mathbf{e}_{\text{out}}} \tilde{\phi}_{\text{oct}} + \mathbf{e}_{\text{out}} \times \nabla_{h_{\text{out}}} \tilde{\phi}_{\text{oct}} \right], \quad (\text{A6})$$

$$\frac{1}{h_{\text{out}}} \frac{d\mathbf{h}_{\text{out}}}{dt} = (1 - e_{\text{out}}^2)^{-1/2} \tau_{\text{out}}^{-1} \left[ \mathbf{e}_{\text{out}} \times \nabla_{\mathbf{e}_{\text{out}}} \tilde{\phi}_{\text{oct}} + (1 - e_{\text{out}}^2)^{1/2} \hat{\mathbf{h}}_{\text{out}} \times \nabla_{h_{\text{out}}} \tilde{\phi}_{\text{oct}} \right], \quad (\text{A7})$$

$$I_1 \frac{d\Omega_1}{dt} = h_{\text{in}}(-Y_1 \hat{\mathbf{e}}_{\text{in}} + X_1 \hat{\mathbf{q}}_{\text{in}} + W_1 \hat{\mathbf{h}}_{\text{in}}), \quad (\text{A8})$$

$$I_2 \frac{d\Omega_2}{dt} = h_{\text{in}}(-Y_2 \hat{\mathbf{e}}_{\text{in}} + X_2 \hat{\mathbf{q}}_{\text{in}} + W_2 \hat{\mathbf{h}}_{\text{in}}), \quad (\text{A9})$$

$$\text{where } \tau_{\text{in}} = \frac{m_1 m_2 \sqrt{G(m_1 + m_2) a_{\text{in}}}}{(m_1 + m_2) \phi_0}, \quad \tau_{\text{out}} = \frac{(m_1 + m_2) m_3 \sqrt{G(m_1 + m_2 + m_3) a_{\text{out}}}}{(m_1 + m_2 + m_3) \phi_0}, \quad (\text{A10})$$

and the gradients are taken over the dimensionless potential  $\tilde{\phi}_{\text{oct}} \equiv \phi_{\text{oct}}/\phi_0$  (Eqs. [A18]-[A21]).

The terms due to tidal effects and rotation can be expressed for  $m_1$  as

$$V_1 = \frac{9}{t_{F1}} \left[ \frac{1 + (15/4)e_{\text{in}}^2 + (15/8)e_{\text{in}}^4 + (5/64)e_{\text{in}}^6}{(1 - e_{\text{in}}^2)^{13/2}} - \frac{11\Omega_{1h}}{18\dot{l}_{\text{in}}} \frac{1 + (3/2)e_{\text{in}}^2 + (1/8)e_{\text{in}}^4}{(1 - e_{\text{in}}^2)^5} \right], \quad (\text{A11})$$

$$W_1 = \frac{1}{t_{F1}} \left[ \frac{1 + (15/2)e_{\text{in}}^2 + (45/8)e_{\text{in}}^4 + (5/16)e_{\text{in}}^6}{(1 - e_{\text{in}}^2)^{13/2}} - \frac{\Omega_{1h}}{\dot{l}_{\text{in}}} \frac{1 + 3e_{\text{in}}^2 + (3/8)e_{\text{in}}^4}{(1 - e_{\text{in}}^2)^5} \right], \quad (\text{A12})$$

$$X_1 = -\frac{m_2 k_1 R_1^5}{\mu \dot{l}_{\text{in}} a_{\text{in}}^5} \frac{\Omega_{1h} \Omega_{1e}}{(1 - e_{\text{in}}^2)^2} - \frac{\Omega_{1q}}{2\dot{l}_{\text{in}} t_{F1}} \frac{1 + (9/2)e_{\text{in}}^2 + (5/8)e_{\text{in}}^4}{(1 - e_{\text{in}}^2)^5}, \quad (\text{A13})$$

$$Y_1 = -\frac{m_2 k_1 R_1^5}{\mu \dot{l}_{\text{in}} a_{\text{in}}^5} \frac{\Omega_{1h} \Omega_{1q}}{(1 - e_{\text{in}}^2)^2} + \frac{\Omega_{1e}}{2\dot{l}_{\text{in}} t_{F1}} \frac{1 + (3/2)e_{\text{in}}^2 + (1/8)e_{\text{in}}^4}{(1 - e_{\text{in}}^2)^5}, \quad (\text{A14})$$

$$Z_1 = \frac{m_2 k_1 R_1^5}{\mu \dot{l}_{\text{in}} a_{\text{in}}^5} \left[ \frac{2\Omega_{1h}^2 - \Omega_{1q}^2 - \Omega_{1e}^2}{2(1 - e_{\text{in}}^2)^2} + \frac{15Gm_2}{a_{\text{in}}^3} \frac{1 + (3/2)e_{\text{in}}^2 + (1/8)e_{\text{in}}^4}{(1 - e_{\text{in}}^2)^5} \right], \quad (\text{A15})$$

where analogous equations are written for  $m_2$  by swapping indices. Considering dissipation in  $m_1$ , the tidal friction timescale is defined in terms of the viscous timescale  $t_{V1}$  and

$$t_{F1} = \frac{t_{V1}}{9} \left( \frac{a_{\text{in}}}{R_1} \right)^8 \frac{m_1^2}{(m_1 + m_2)m_2} (1 + 2k_1)^{-2}. \quad (\text{A16})$$

Here,  $k_1$  is the classical apsidal motion constant, a measure of quadrupolar deformability which is related to the Love number  $k_L$  and the coefficient  $Q_E$  given by Eggleton & Kiseleva-Eggleton (2001):  $k_1 = k_L/2 = \frac{1}{2}Q_E/(1 - Q_E)$ . We use  $k_1 = 0.014$ , valid for  $n = 3$  polytropes, to represent the host star and  $k_2 = 0.25$ , valid for  $n = 1$  polytropes, to represent gas giant planets.

Additionally,  $Z_{\text{GR}}$  is the GR precession rate given by

$$Z_{\text{GR}} = \frac{3G^{3/2}(m_1 + m_2)^{3/2}}{a_{\text{in}}^{5/2} c^2 (1 - e_{\text{in}}^2)}. \quad (\text{A17})$$

The gradients of the dimensionless potential  $\tilde{\phi}_{\text{oct}} = \phi_{\text{oct}}/\phi_0$  are

$$\begin{aligned} \nabla_{\mathbf{e}_{\text{in}}} \tilde{\phi}_{\text{oct}} = & -\frac{1}{(1 - e_{\text{out}}^2)^{3/2}} \left\{ 5(\mathbf{e}_{\text{in}} \cdot \hat{\mathbf{h}}_{\text{out}}) - 2\epsilon_{\text{oct}} \left[ 7(\mathbf{e}_{\text{in}} \cdot \hat{\mathbf{h}}_{\text{out}})(\mathbf{e}_{\text{in}} \cdot \hat{\mathbf{e}}_{\text{out}}) - (1 - e_{\text{in}}^2)(\hat{\mathbf{h}}_{\text{in}} \cdot \hat{\mathbf{h}}_{\text{out}})(\hat{\mathbf{h}}_{\text{in}} \cdot \hat{\mathbf{e}}_{\text{out}}) \right] \right\} \hat{\mathbf{h}}_{\text{out}} \\ & + \frac{\epsilon_{\text{oct}}}{(1 - e_{\text{out}}^2)^{3/2}} \left[ \left( \frac{1}{5} - \frac{8}{5}e_{\text{in}}^2 \right) - (1 - e_{\text{in}}^2)(\hat{\mathbf{h}}_{\text{in}} \cdot \hat{\mathbf{h}}_{\text{out}})^2 + 7(\mathbf{e}_{\text{in}} \cdot \hat{\mathbf{h}}_{\text{out}})^2 \right] \hat{\mathbf{e}}_{\text{out}} \\ & + \frac{2}{(1 - e_{\text{out}}^2)^{3/2}} \left[ 1 - \frac{8}{5}\epsilon_{\text{oct}}(\mathbf{e}_{\text{in}} \cdot \hat{\mathbf{e}}_{\text{out}}) \right] \mathbf{e}_{\text{in}}, \end{aligned} \quad (\text{A18})$$

$$\begin{aligned} \nabla_{\mathbf{h}_{\text{in}}} \tilde{\phi}_{\text{oct}} = & \frac{(1 - e_{\text{in}}^2)^{1/2}}{(1 - e_{\text{out}}^2)^{3/2}} \left\{ (\hat{\mathbf{h}}_{\text{in}} \cdot \hat{\mathbf{h}}_{\text{out}}) - 2\epsilon_{\text{oct}} \left[ (\mathbf{e}_{\text{in}} \cdot \hat{\mathbf{e}}_{\text{out}})(\hat{\mathbf{h}}_{\text{in}} \cdot \hat{\mathbf{h}}_{\text{out}}) + (\mathbf{e}_{\text{in}} \cdot \hat{\mathbf{h}}_{\text{out}})(\hat{\mathbf{h}}_{\text{in}} \cdot \hat{\mathbf{e}}_{\text{out}}) \right] \right\} \hat{\mathbf{h}}_{\text{out}} \\ & - \frac{2\epsilon_{\text{oct}}(1 - e_{\text{in}}^2)^{1/2}}{(1 - e_{\text{out}}^2)^{3/2}} (\hat{\mathbf{h}}_{\text{in}} \cdot \hat{\mathbf{h}}_{\text{out}})(\mathbf{e}_{\text{in}} \cdot \hat{\mathbf{h}}_{\text{out}}) \hat{\mathbf{e}}_{\text{out}}, \end{aligned} \quad (\text{A19})$$

$$\begin{aligned}
\nabla_{e_{\text{out}}} \tilde{\phi}_{\text{oct}} = & \frac{5}{(1 - e_{\text{out}}^2)^{5/2}} \left[ \frac{1}{2} (1 - e_{\text{in}}^2) (\hat{\mathbf{h}}_{\text{in}} \cdot \hat{\mathbf{h}}_{\text{out}})^2 + \frac{3}{5} \left( e_{\text{in}}^2 - \frac{1}{6} \right) - \frac{5}{2} (\mathbf{e}_{\text{in}} \cdot \hat{\mathbf{h}}_{\text{out}})^2 \right] \hat{\mathbf{e}}_{\text{out}} \\
& + \frac{7\epsilon_{\text{oct}}}{(1 - e_{\text{out}}^2)^{5/2}} \left\{ (\mathbf{e}_{\text{in}} \cdot \hat{\mathbf{e}}_{\text{out}}) \left[ \left( \frac{1}{7} - \frac{8}{7} e_{\text{in}}^2 \right) - (1 - e_{\text{in}}^2) (\hat{\mathbf{h}}_{\text{in}} \cdot \hat{\mathbf{h}}_{\text{out}})^2 + 7 (\mathbf{e}_{\text{in}} \cdot \hat{\mathbf{h}}_{\text{out}})^2 \right] \right. \\
& \left. - 2(1 - e_{\text{in}}^2) (\hat{\mathbf{h}}_{\text{in}} \cdot \hat{\mathbf{h}}_{\text{out}}) (\mathbf{e}_{\text{in}} \cdot \hat{\mathbf{h}}_{\text{out}}) (\hat{\mathbf{h}}_{\text{in}} \cdot \hat{\mathbf{e}}_{\text{out}}) \right\} \hat{\mathbf{e}}_{\text{out}} \\
& + \frac{\epsilon_{\text{oct}}}{e_{\text{out}} (1 - e_{\text{out}}^2)^{3/2}} \left[ \left( \frac{1}{5} - \frac{8}{5} e_{\text{in}}^2 \right) - (1 - e_{\text{in}}^2) (\hat{\mathbf{h}}_{\text{in}} \cdot \hat{\mathbf{h}}_{\text{out}})^2 + 7 (\mathbf{e}_{\text{in}} \cdot \hat{\mathbf{h}}_{\text{out}})^2 \right] \mathbf{e}_{\text{in}} \\
& - \frac{2\epsilon_{\text{oct}} (1 - e_{\text{in}}^2)}{e_{\text{out}} (1 - e_{\text{out}}^2)^{3/2}} (\hat{\mathbf{h}}_{\text{in}} \cdot \hat{\mathbf{h}}_{\text{out}}) (\mathbf{e}_{\text{in}} \cdot \hat{\mathbf{h}}_{\text{out}}) \hat{\mathbf{h}}_{\text{in}}, \tag{A20}
\end{aligned}$$

$$\begin{aligned}
\nabla_{h_{\text{out}}} \tilde{\phi}_{\text{oct}} = & \frac{(1 - e_{\text{in}}^2)}{(1 - e_{\text{out}}^2)^2} \left\{ (\hat{\mathbf{h}}_{\text{in}} \cdot \hat{\mathbf{h}}_{\text{out}}) - 2\epsilon_{\text{oct}} \left[ (\mathbf{e}_{\text{in}} \cdot \hat{\mathbf{e}}_{\text{out}}) (\hat{\mathbf{h}}_{\text{in}} \cdot \hat{\mathbf{h}}_{\text{out}}) + (\mathbf{e}_{\text{in}} \cdot \hat{\mathbf{h}}_{\text{out}}) (\hat{\mathbf{h}}_{\text{in}} \cdot \hat{\mathbf{e}}_{\text{out}}) \right] \right\} \hat{\mathbf{h}}_{\text{in}} \\
& - \frac{1}{(1 - e_{\text{out}}^2)^2} \left\{ 5 (\mathbf{e}_{\text{in}} \cdot \hat{\mathbf{h}}_{\text{out}}) - 2\epsilon_{\text{oct}} \left[ 7 (\mathbf{e}_{\text{in}} \cdot \hat{\mathbf{e}}_{\text{out}}) (\mathbf{e}_{\text{in}} \cdot \hat{\mathbf{h}}_{\text{out}}) - (1 - e_{\text{in}}^2) (\hat{\mathbf{h}}_{\text{in}} \cdot \hat{\mathbf{h}}_{\text{out}}) (\hat{\mathbf{h}}_{\text{in}} \cdot \hat{\mathbf{e}}_{\text{out}}) \right] \right\} \mathbf{e}_{\text{in}}. \tag{A21}
\end{aligned}$$

## TIME-AVERAGED ECCENTRICITY DISTRIBUTION OVER A KOZAI-LIDOV CYCLE

The averaged Hamiltonian that represents the gravitational interaction up to the quadrupole approximation (Eq. A3 with  $\epsilon_{\text{oct}} = 0$ ) can be written in terms of the orbital elements as

$$H_q = \frac{\phi_0}{6(1 - e_{\text{out}}^2)^{3/2}} [2 + 3e_{\text{in}}^2 - (3 - 3e_{\text{in}}^2 + 15e_{\text{in}}^2 \sin^2 \omega_{\text{in}}) \sin^2 i_{\text{tot}}], \tag{B1}$$

where  $i_{\text{tot}}$  is the angle between  $\mathbf{h}_{\text{in}}$  and  $\mathbf{h}_{\text{out}}$  (Eqs. A1-A2) and  $\omega_{\text{in}}$  is the argument of pericenter of the inner orbit.

In the limit of the outer body having all the angular momentum (i.e.,  $h_{\text{in}} \ll h_{\text{out}}$ ) the vector  $\mathbf{h}_{\text{out}}$  remains fixed and we can use it to define a reference frame in which  $i_{\text{tot}} \equiv i_{\text{in}}$ .

Let us fix the energy by setting  $e_{\text{in}} = e_0$ ,  $i_{\text{in}} = i_0$ , and  $\omega_{\text{in}} = \omega_0$ :

$$H_{q,0} = \frac{\phi_0}{6(1 - e_{\text{out}}^2)^{3/2}} (2 + 3\theta_0), \text{ where } \theta_0 \equiv e_0^2 - (1 - e_0^2 + 5e_0^2 \sin^2 \omega_0) \sin^2 i_0. \tag{B2}$$

We can now write the distribution function as

$$\begin{aligned}
f(\omega_{\text{in}}, \Omega_{\text{in}}, G_{\text{in}}, H_{\text{in}}) = & \delta(H_q - H_{q,0}) \\
& \propto \delta[e_{\text{in}}^2 - (1 - e_{\text{in}}^2 + 5e_{\text{in}}^2 \sin^2 \omega_{\text{in}}) \sin^2 i_{\text{in}} - \theta_0]. \tag{B3}
\end{aligned}$$

Let us define the dimensionless momenta  $\tilde{G}_{\text{in}} = G_{\text{in}}/L_{\text{in}} = \sqrt{1 - e_{\text{in}}^2}$  and  $\tilde{H}_{\text{in}} = H_{\text{in}}/L_{\text{in}} = \sqrt{1 - e_{\text{in}}^2} \cos i_{\text{in}}$ , where the latter is a constant of motion (i.e.,  $\tilde{H}_{\text{in}} = \sqrt{1 - e_0^2} \cos i_0$ ) because the Hamiltonian is independent of the longitude of the ascending node  $\Omega_{\text{in}}$ . This allows us to express the time-averaged eccentricity distribution as

$$n_e(e_{\text{in}}|\theta_0, \tilde{H}_{\text{in}}) \propto \int \int d\tilde{G}_{\text{in}} d\omega_{\text{in}} \delta \left[ e_{\text{in}}^2 - (1 - e_{\text{in}}^2 + 5e_{\text{in}}^2 \sin^2 \omega_{\text{in}}) \left( 1 - \frac{\tilde{H}_{\text{in}}^2}{\tilde{G}_{\text{in}}^2} \right) - \theta_0 \right] \delta \left( e_{\text{in}} - \sqrt{1 - \tilde{G}_{\text{in}}^2} \right), \tag{B4}$$

and integrating over  $\tilde{G}_{\text{in}}$  we get

$$n_e(e_{\text{in}}|\theta_0, \tilde{H}_{\text{in}}) \propto \int d\omega_{\text{in}} \frac{e_{\text{in}}}{(1 - e_{\text{in}}^2)^{1/2}} \delta \left[ e_{\text{in}}^2 - (1 - e_{\text{in}}^2 + 5e_{\text{in}}^2 \sin^2 \omega_{\text{in}}) \left( 1 - \frac{\tilde{H}_{\text{in}}^2}{1 - e_{\text{in}}^2} \right) - \theta_0 \right] \tag{B5}$$

$$\propto \frac{e_{\text{in}}}{\left\{ \left[ 2e_{\text{in}}^2 + \tilde{H}_{\text{in}}^2 - \theta_0 - 1 \right] \left[ (1 + 4e_{\text{in}}^2) \left( 1 - e_{\text{in}}^2 - \tilde{H}_{\text{in}}^2 \right) - (e_{\text{in}}^2 - \theta_0) (1 - e_{\text{in}}^2) \right] \right\}^{1/2}}, \tag{B6}$$

which is defined for  $e_{\text{in}} \in [0, 1]$  such that  $n_e(e_{\text{in}}|\theta_0, \tilde{H}_{\text{in}})$  is real and can be normalized to 1 as:  $\int_0^1 de_{\text{in}} n(e_{\text{in}}|\theta_0, \tilde{H}_{\text{in}}) = 1$ . We checked that this distribution matches the time-averaged eccentricity distribution obtained from solving the Equations (A4)-(A5) when  $\epsilon_{\text{oct}} = 0$  and no extra forces are included.

A relevant limit for this work is to start with a planet in a low-eccentricity orbit ( $e_0^2 \ll 1$ ) and a stellar companion with inclination  $i_0$ , so  $\theta_0 \rightarrow -\sin^2 i_0$  and  $\tilde{H}_{\text{in}} \rightarrow \cos i_0$ . This limit simplifies the Equation (B6) to

$$n_e(e_{\text{in}}|i_0) \propto \frac{1}{e_{\text{in}} \left[ \frac{3}{5}(1 - e_{\text{in}}^2) - \cos^2 i_0 \right]^{1/2}}, \quad (\text{B7})$$

where the eccentricity distribution is defined for a minimum eccentricity, say  $e \sim 0.01$ , and  $\cos^2 i_0 < \frac{3}{5}(1 - e_{\text{in}}^2)$ . The latter condition implies that KL oscillations are restricted to  $|\cos i_0| < \sqrt{3/5}$  and the maximum eccentricity is given by  $\sqrt{1 - 5/3 \cos^2 i_0}$ .

In contrast, by restricting to the initial high-inclination case  $i_0 \simeq \pi/2$  and setting  $\omega_0 = \pi/2$  (or  $3\pi/2$ ) we can define the minimum eccentricity  $e_{\text{min}} = e_0$  and the maximum eccentricity  $e_{\text{max}} = \sqrt{1 - 5/3 \cos^2 i_0}$ . Conveniently, this distribution only depends only on  $e_{\text{min}}$  and  $e_{\text{max}}$ :

$$n_e(e_{\text{in}}|e_{\text{min}}, e_{\text{max}}) \equiv n_e(e_{\text{in}}|\theta_0(e_{\text{min}}, e_{\text{max}}), \tilde{H}_{\text{in}}(e_{\text{min}}, e_{\text{max}})), \text{ where} \\ \theta_0(e_{\text{min}}, e_{\text{max}}) = e_{\text{min}}^2 - \frac{1}{5} (1 + 4e_{\text{min}}^2) (2 + 3e_{\text{max}}^2), \quad \tilde{H}_{\text{in}}(e_{\text{min}}, e_{\text{max}}) = \sqrt{\frac{3}{5} (1 - e_{\text{min}}^2) (1 - e_{\text{max}}^2)}, \quad (\text{B8})$$

which simplifies our analysis in §2.3.

## REFERENCES

- Antognini, J. M., Shappee, B. J., Thompson, T. A., & Amaro-Seoane, P. 2014, *MNRAS*, 439, 1
- Antonini, F., Murray, N., & Mikkola, S., 2014, *ApJ*, 781, 45
- Albrecht, S., Winn, J. N., Johnson, J. A., et al. 2012, *ApJ*, 757, 18
- Beaugé, C., & Nesvorný, D. 2012, *ApJ*, 751, 119
- Bodenheimer, P., Laughlin, G., & Lin, D. N. C. 2003, *ApJ*, 592, 555
- Bodenheimer, P., Lin, D. N. C., & Mardling, R. A. 2001, *ApJ*, 548, 466
- Burrows, A., Marley, M., Hubbard, W. B., et al. 1997, *ApJ*, 491, 856
- Butler, R. P., Wright, J. T., Marcy, G. W., et al. 2006, *ApJ*, 646, 505
- Correia, A. C. M., Laskar, J., Farago, F., & Boué, G. 2011, *CeMDA*, 111, 105
- Cumming, A. 2004, *MNRAS*, 354, 1165
- Cumming, A., Butler, R. P., Marcy, G. W., et al. 2008, *PASP*, 120, 531
- Dawson, R., Murray-Clay, R. A., & Johnson, J. A. 2012, *arXiv:1211.0554*
- Dawson, R. I., & Johnson, J. A. 2012, *ApJ*, 756, 122
- Dawson, R., & Murray-Clay, R. A. 2013, *ApJL*, 767, L24
- Dawson, R. 2014, *ApJL*, 790, L31
- Desidera, S., & Barbieri, M. 2007, *A&A*, 462, 345
- Dong, S., Katz, B., & Socrates, A. 2014, *ApJ*, 781, 1
- Duquennoy, A., & Mayor, M. 1991, *A&A*, 248, 485
- Eggenberger, A., Udry, S., Chauvin, G., et al. 2011, in *IAU Symp. 276, The Astrophysics of Planetary Systems: Formation, Structure, and Dynamical Evolution*, ed. A. Sozzetti, M. G. Lattanzi, & A. P. Boss (Cambridge: Cambridge Univ. Press), 409
- Eggleton, P. P., Kiseleva, L. G., & Hut, P. 1998, *ApJ*, 499, 853
- Eggleton, P. P., & Kiseleva-Eggleton, L. 2001, *ApJ*, 562, 1012
- Faber, J. A., Rasio, F. A., & Willems, B. 2005, *Icarus*, 175, 248
- Fabrycky, D., & Tremaine, S. 2007, *ApJ*, 669, 1298
- Fabrycky, D., & Winn, J. 2009, *ApJ*, 696, 1230
- Farago, F., & Laskar, J. 2010, *MNRAS*, 2, 1189
- Ford, E. B., Kozinsky, B., & Rasio, F. A. 2000, *ApJ*, 535, 385
- Gaudi, B. S., Seager, S., & Mallen-Ornelas, G. 2005, *ApJ*, 623, 472
- Goldreich, P., & Soter, S. 1966, *Icarus*, 5, 375
- Gould, A., Dorsher, S., Gaudi, B. S., & Udalski, A. 2006, *AcA*, 56, 1
- Gu, P.-G., Lin, D. N. C., & Bodenheimer, P. H. 2003, *ApJ*, 588, 509
- Guillochon, J., Ramirez-Ruiz, E., & Lin, D. 2011, *ApJ*, 732, 74
- Hale, A. 1994, *AJ*, 107, 306
- Hansen, B. M. S. 2010, *ApJ*, 723, 285
- Hansen, B. M. S. 2012, *ApJ*, 757, 6
- Holman, M., Touma, J., & Tremaine, S. 1997, *Nature*, 386, 254
- Holman, M. J., & Wiegert, P. A. 1999, *AJ*, 117, 621
- Howard, A. W., Marcy, G. W., Bryson, S. T., et al. 2012, *ApJS*, 201, 15
- Hut, P. 1981, *A&A*, 99, 126
- Innanen, K. A., Zheng, J. Q., Mikkola, S., & Valtonen, M. J. 1997, *AJ*, 113, 1915
- Ivanov, P. B., & Papaloizou, J. C. B. 2004, *MNRAS*, 347, 437
- Ivanov, P. B., & Papaloizou, J. C. B. 2011, *Celestial Mechanics and Dynamical Astronomy*, 111, 51
- Ivanov, P. B., Polnarev, A. G., & Saha, P. 2005, *MNRAS*, 358, 1361
- Jackson, B., Greenberg, R., & Barnes, R. 2009, *ApJ*, 698, 1357
- Jensen, E. L. N., Mathieu, R. D., Donar, A. X., & Dullighan, A. 2004, *ApJ*, 600, 789
- Jensen, E. L. N., & Akeson, R. 2014, *Nature*, 511, 567
- Katz, B., Dong, S., & Malhotra, R. 2011, *PhRvL*, 107, 181101
- Kiseleva, L. G., Eggleton, P. P., & Mikkola, S. 1998, *MNRAS*, 300, 292
- Kozai, Y. 1962, *AJ*, 67, 591
- Lai, D. 1997, *ApJ*, 490, 847
- Lai, D., 2012, *MNRAS*, 423, 486
- Laine, V., Arlot, J.-E., Karatekin, O., & van Hoolst, T. 2009, *Nature*, 459, 957
- Law, N. M., Morton, T. D., Baranec, C. et al. 2014, *ApJ*, 791, 35
- Leconte, J., Chabrier, G., Baraffe, I., & Levrard, B. 2010, *A&A*, 516, A64
- Levrard, B., Winnisoerffer, C., & Chabrier, G. 2009, *ApJ*, 692, 9
- Li, G., Naoz, S., Bence, K., & Loeb, A. 2014, *ApJ*, 785, 116
- Lidov, M. L. 1962, *P&SS*, 9, 719
- Lithwick, Y., & Naoz, S. 2011, *ApJ*, 742, 94
- Liu, S.-F., Guillochon, J., Lin, D. N. C., & Ramirez-Ruiz, E. 2012, *ApJ*, 762, 37
- Marcy, G., Butler, R. P., Fischer, D., et al. 2005, *Prog. Theor. Phys. Suppl.*, 158, 24
- Mardling, R. A., & Aarseth, S. J. 2001, *MNRAS*, 321, 398
- Martí, J. G., & Beaugé, C. 2014, *arXiv:1403.3056*
- Mayor, M., et al. 2011, *arXiv:1109.2497*
- Metzger, B. D., Giannios, D., & Spiegel, D. S. 2012, *MNRAS*, 425, 2778
- Morton, T. D., & Johnson, J. A. 2011, *ApJ*, 729, 138
- Monin, J., Ménard, F., & Peretto, N. 2006, *A&A*, 446, 201
- Mugrauer, M., & Neuhauser, R. 2009, *A&A*, 494, 373
- Naef, D., et al. 2001, *A&A*, 375, L27
- Naoz, S., Bence, K., Loeb, A., & Nicolás, Y. 2013b, *ApJ*, 773, 187
- Naoz, S., Farr, W. M., Lithwick, Y., Rasio, F. A., & Teyssandier, J. 2011, *Nature*, 473, 187
- Naoz, S., Farr, W. M., Lithwick, Y., Rasio, F. A., & Teyssandier, J. 2013, *MNRAS*, 431, 2155
- Naoz, S., Farr, W. M., & Rasio, F. A. 2012, *ApJ*, 754, L36
- O'Toole, S. J., Tinney, C. G., Jones, H. R. A., et al. 2009, *MNRAS*, 392, 641
- Petrovich, C. 2014, *arXiv:1409.8296*

- Quinn, S. N. , White, R. J., Latham, D. W., et al., 2014, *ApJ*, 787, 27
- Raghavan, D., McAlister, H. A., Henry, T. J., et al. 2010, *ApJS*, 190, 1
- Rogers, T. M. & Lin, D. N. C. 2013, *ApJ*, 769, L10
- Socrates, A., Katz, B., & Dong, S. 2012a, arXiv:1209.5724
- Socrates, A., Katz, B., Dong, S., & Tremaine, S. 2012b, *ApJ*, 750, 106
- Storch, N. I., & Lai, D. 2014, *MNRAS*, 438, 2
- Storch, N. I., Anderson, K. R., & Lai, D. 2014, *Science*, 345, 1317
- Takeda, G., & Rasio, F. A. 2005, *ApJ*, 627, 1001
- Tremaine, S., Touma, J., & Namouni, F. 2009, *AJ*, 137, 3706
- Tremaine, S. & Yavetz, T. 2014, *AJP*, 82, 8
- Udry, S., & Santos, N. C. 2007, *ARA&A*, 45, 397
- Valsecchi, F. & Rasio, F.A. 2014a, *ApJ*, 786, 102
- Valsecchi, F., & Rasio, F. A. 2014b, *ApJ*, 787, L9
- Yoder, C. F., & Peale, S. J. 1981, *Icarus*, 47, 1
- Walkowicz, L. M., & Basri, G. S. 2013, *MNRAS*, 436, 1883
- Williams, J., Rita, K., Mann, R. K., Francesco, J. D., et al. 2014, *ApJ*, 796, 120
- Wright J. T. et al. 2011, *PASP*, 123, 412
- Wright, J. T., Marcy, G. W., Howard, A. W., et al. 2012, *ApJ*, 753, 160
- Wu, Y. & Murray, N. 2003, *ApJ*, 589, 605
- Wu, Y., Murray, N. W., & Ramsahai, J. M., 2007, *ApJ*, 670, 820
- Zakamska, N. L., Pan, M., & Ford, E. B. 2011, *MNRAS*, 410, 1895
- Zucker, S., & Mazeh, T. 2002, *ApJ*, 568, L113